


2016

Characterization of Dispersion and Residual Stress in Nanoparticle Reinforced Hybrid Carbon Fiber Composites

Alex Selimov
University of Central Florida

 Part of the [Structural Materials Commons](#), and the [Structures and Materials Commons](#)
Find similar works at: <https://stars.library.ucf.edu/honorsthesis>
University of Central Florida Libraries <http://library.ucf.edu>

This Open Access is brought to you for free and open access by the UCF Theses and Dissertations at STARS. It has been accepted for inclusion in Honors Undergraduate Theses by an authorized administrator of STARS. For more information, please contact STARS@ucf.edu.

Recommended Citation

Selimov, Alex, "Characterization of Dispersion and Residual Stress in Nanoparticle Reinforced Hybrid Carbon Fiber Composites" (2016). *Honors Undergraduate Theses*. 233.
<https://stars.library.ucf.edu/honorsthesis/233>

CHARACTERIZATION OF DISPERSION AND RESIDUAL STRESS
IN NANOPARTICLE REINFORCED HYBRID CARBON FIBER
COMPOSITES

by

ALEX SELIMOV

A thesis submitted in partial fulfillment of the requirements
for the Honors in the Major Program in Mechanical Engineering
in the College of Engineering and Computer Science
at the University of Central Florida
Orlando, Florida

Fall Term, 2016

Thesis Chair: Dr. Seetha Raghavan

© 2016 by Alex Selimov

ABSTRACT

Hybrid carbon fiber reinforced composites are a new breed of materials that are currently being explored and characterized for next generation aerospace applications [1]. Through the introduction of secondary reinforcements, such as alumina nanoparticles, hybrid properties including improved mechanical properties and stress sensing capabilities can be achieved. In order to maximize these properties, it is necessary to achieve a homogeneous dispersion of particulate filler. Utilizing the photoluminescent properties of alumina, it is possible to compare local levels of particle concentration through emission intensities as a way to determine the effectiveness of the tested manufacturing parameters in increasing material homogeneity. Parameters of these photoluminescence emissions have been established to be stress dependent, which allows for *in situ* residual stress measurements. It is shown here that the application of silane coupling agents as particle surface treatments improves particle dispersion when compared to untreated samples. Reactive silane coupling agent (RSCA) treatments were found to provide for greater dispersion improvements when compared to non-reactive silane coupling agents (NRSCA). Higher resolution investigations into these samples found that treatment with a reactive coupling agent altered the stress state of particles concentrated around the fiber from a tensile stress state to a compressive stress state. This is proposed to result from bonding of the reactive groups on the coupling agent to the organic groups on the carbon fibers which adjusts the stress state of the particle. Future mechanical tests will verify the effects of the particle surface functionalization treatments on mechanical properties of the composites.

DEDICATION

This work is dedicated to my mother. Without her love and endless support I would never have been where I am today.

ACKNOWLEDGMENTS

My sincere gratitude goes out to my committee chair and research advisor Dr. Seetha Raghavan for her guidance and support throughout my undergraduate research efforts which culminated in this work. I would like to thank my thesis committee members, Dr. Yuanli Bai and Dr. Axel Schülzgen, for supporting this endeavor. I also thank members of my research team, especially Albert Manero and Dr. Gregory Freihofer, for supporting this research and providing invaluable mentorship.

I acknowledge Dr. Ambrose Taylor and Dr. Declan Carolan from Imperial College London for their contribution to this work through the manufacturing of the tested samples. I also acknowledge Dr. Laurene Tetard and Yi Ding from the UCF Nanoscience Technology Center for their support with the collection of some of the data presented. Finally, I acknowledge the National Science Foundation's Innovation through Institutionalized Integration (ICubed) for providing support during my time as an undergraduate research assistant. This material is based upon work supported by the National Science Foundation under Grant No. 1130837.

TABLE OF CONTENTS

LIST OF FIGURES	ix
LIST OF TABLES	xiii
CHAPTER 1 INTRODUCTION	1
1.1 Motivation	1
1.2 Hybrid Carbon Fiber Reinforced Polymer Composites (HCFRPs)	2
1.3 Nanoparticle Reinforcement and Agglomeration	3
1.4 Silane Coupling Agents	4
1.5 Residual Stress in Composites	6
CHAPTER 2 OPTICAL SPECTROSCOPY OF Cr ³⁺	8
2.1 Photoluminescence mechanisms in alumina	8
2.1.1 Photoluminescence Mapping	9
2.2 Piezospectroscopy	11
2.2.1 Piezospectroscopic Mapping	12

CHAPTER 3	EXPERIMENTAL METHODS	14
3.1	Photoluminescence Collections	14
3.1.1	Portable Piezospectroscopy System	14
3.1.2	High Resolution Investigations	16
3.1.3	R-line processing and analysis	18
3.2	Sample Manufacturing	20
3.2.1	Nanoparticle/Polymer Mixture	21
3.2.2	Infusion of Carbon Fibers	22
3.2.3	Sample Design	23
CHAPTER 4	PARTICLE DISPERSION ANALYSIS	25
4.1	Qualitative Analysis of Weight Percentage Effects on Particle Dispersion	25
4.1.1	Untreated Dispersion Behavior with Increasing Weight Percentage	26
4.1.2	Surface Treatment Effects on Dispersion Behavior	28
4.2	Quantitative Analysis of Dispersion and Sedimentation	30
4.2.1	Conversion of contour plots to intensity distributions	31
4.2.2	Dispersion Characterization through Variance to Mean Ratio	34

4.2.3 Sedimentation Analysis	38
4.3 Conclusions	40
CHAPTER 5 PARTICLE BONDING INVESTIGATION	43
5.1 Untreated Particle Behavior	44
5.2 Functionalization of Particles for Adjustment of Bonding Behavior	46
5.3 Conclusion	49
CHAPTER 6 CONCLUSION	50
LIST OF REFERENCES	52

LIST OF FIGURES

1.1	Schematic showing applications of hybrid carbon fiber composites for aerospace applications, improving material properties and allowing for stress sensing.	2
1.2	Schematic for energy dissipation mechanism through crack deflection resulting from the presence of secondary reinforcements. [2]	3
1.3	Schematic for SCA coupling processes: a) Hydrolyzable groups on alumina surface react with hydrolyzable groups on SCA to form b) covalent bond between particle surface and SCA treatment, c) bonding of SCA to organic matrix through various process.]	5
2.1	Schematic of photoluminescence mechanisms in Cr^{3+} . Initial laser impingement causes an excitation of electrons to a higher energy state. The energy state necessary for the emission of photons is reached through a nonradiative transition.	9
2.2	PL intensity map with data schematic showing local variations in intensity corresponding to particle dispersion [3].	10
2.3	PL peak shift map with data schematic showing local variations in wavenumber corresponding to local stress state. Values can be converted to stress through application of the PS equation [4].	13

3.1	Schematic for equipment used to collect and track photoluminescence emissions from aluminum oxide.	15
3.2	Different laser spot sizes allow for different spatial resolution for the collection of intensity and piezospectroscopic data [5].	17
3.3	Transformation of raw spectral data to individual pseudo-Voigt functions and fitted doublet [6].	18
3.4	Schematic outlining manufacturing of hybrid carbon fiber composite sheets through the resin infusion under flexible tooling (RIFT) process. A schematic outlining resin guidance with flow media is also presented.	23
3.5	a) Schematic of design with labeled dimensions and b) image of sample tested .	24
4.1	Dispersion maps for untreated sample showing increased particle agglomeration with highest particle loading.	26
4.2	Low concentration lines in 9 wt% untreated samples where the white arrows indicate direction.	27
4.3	RSCA treated sample dispersion maps showcasing consistent intensities across surfaces with presence of small agglomerations.	29
4.4	Dispersion maps for NRSCA treated samples. Large agglomeration behavior is present in 9 and 12 wt% samples.	30
4.5	Schematic outlining intensity distributions for well dispersed and poorly dispersed samples [3].	31

4.6	Intensity distributions for a) Untreated samples, b) RSCA treated samples, c) NRSCA treated samples, and d) a schematic outlining good dispersion and poor dispersion.	32
4.7	Two examples of of previously presented intensity distribution histograms plotted against the standard random distribution of data at the same mean, which is represented by the Poisson's distribution. Plot a) is seen to have a more random distribution than plot b) and a lower VMR.	35
4.8	VMR plotted for both sets of each sample. The lines represent the overall average VMR in order to highlight the optimal overall dispersion and variations in dispersion between volume fractions. The RSCA treatment provides the most consistent improvements to dispersion and is found to be the most independent of manufacturing parameters	37
4.9	Sedimentation coefficient for each sample calculated by comparing difference in surface intensities between samples	39
5.1	Micrograph image focused on single fiber shows outer matrix regions as being out of focus.	44
5.2	Residual stress behavior of particles treated with no surface treatment.a) Micrograph image overlaid with intensity plots showing particle alignment with fiber direction and b) (top) Intensity gradients correlating with (middle) hydrostatic residual stress gradients and (bottom) FWHM gradients	45

5.3 Residual stress behavior of particles treated with NRSCA surface treatment.
a) Micrograph image overlaid with intensity plots showing particle alignment with fiber direction and b) (top) Intensity gradients correlating with (middle) hydrostatic residual stress gradients and (bottom) FWHM gradients 47

5.4 Residual stress behavior of particles treated with RSCA surface treatment. a) Micrograph image overlaid with intensity plots showing particle alignment with fiber direction and b) (top) Intensity gradients correlating with (middle) hydrostatic residual stress gradients and (bottom) FWHM gradients. 48

LIST OF TABLES

3.1	All combination of manufacturing parameters for the creation of 9 unique samples	21
4.1	VMR for all tested samples. Lowest values for each surface treatment is bolded.	41
4.2	Sedimentation coefficient values for all tested samples. Lowest coefficient value for each treatment type is bolded.	42

CHAPTER 1 INTRODUCTION

1.1 Motivation

Carbon fiber composites hybridized with alumina nanoparticles are promising next generation materials offering improved properties such as fracture toughness [7], crack initiation toughness [8], and elastic modulus [9] among others [10, 11]. However, these benefits are highly dependent on the homogeneous dispersion of the added nanoparticles [12]. Increasing volume fraction of nanoparticle inclusions results in the presence of agglomerations which act as stress concentrators [13] acting to promote earlier failure. Particle dispersion analysis is not a straightforward task, traditional methods require extrapolation of analysis conducted on micrographs of small areas. In work preceding this, photoluminescence spectroscopy has been applied for the investigation of dispersion in alumina reinforced polymer nanocomposites [14] and in hybrid carbon fiber composites [15]. This technique was found to be capable of characterizing particle dispersion based on emission intensities at large scales. In previous hybrid carbon fiber composites, particle loadings above 10 wt% resulted in agglomerations which begin to dominate sample surfaces. Silane coupling agents (SCAs) are explored in this work for improving particle dispersion in order fully utilize the property improvements unlocked from a higher volume fraction of reinforcement. Applying these methods for the characterization of optimal processing parameters uncovers steps for the development of novel hybrid composite with improved material properties and stress sensing capabilities, shown in Figure 1.1.

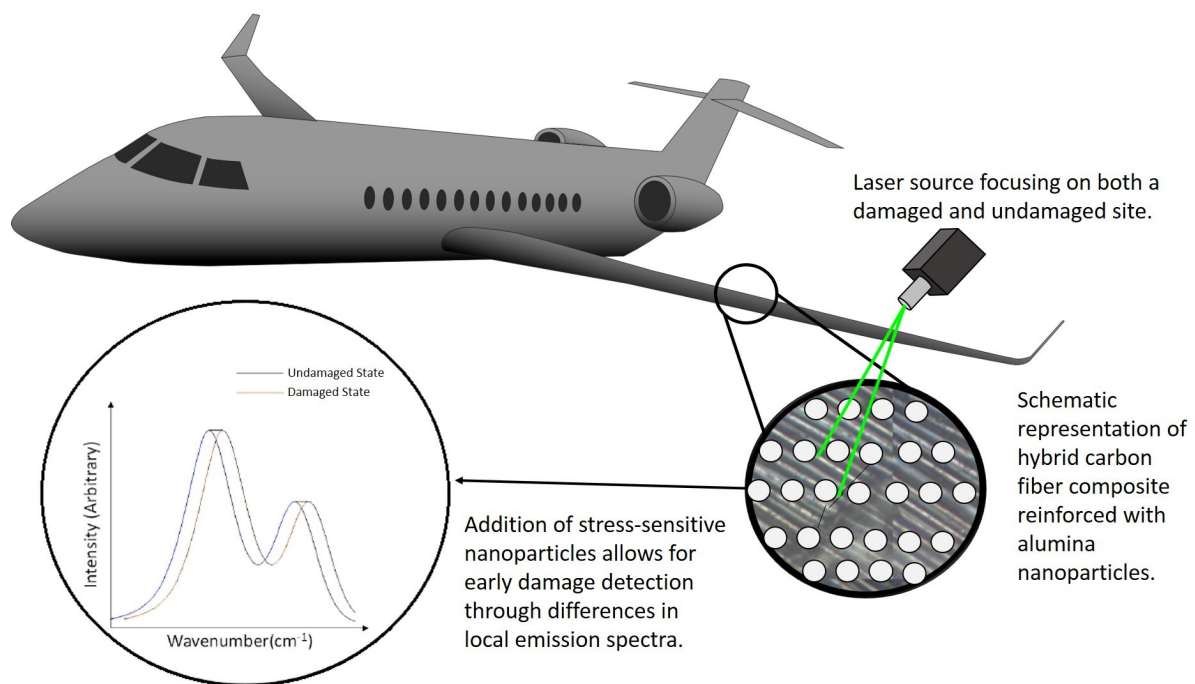


Figure 1.1: Schematic showing applications of hybrid carbon fiber composites for aerospace applications, improving material properties and allowing for stress sensing.

1.2 Hybrid Carbon Fiber Reinforced Polymer Composites (HCFRPs)

Carbon fiber composites are desirable materials for aerospace applications due to their high strength to weight ratio [16]. However, the two component nature of these materials limits property optimizations as manufacturers are forced to select properties on a linear spectrum of possible values [17]. The introduction of a secondary matrix reinforcement is necessary in order to provide for a greater spectrum of selectable material properties [18]. Alumina particles are promising as a secondary reinforcement due to their improvement of mechanical properties such as elastic modulus and fracture toughness [19].

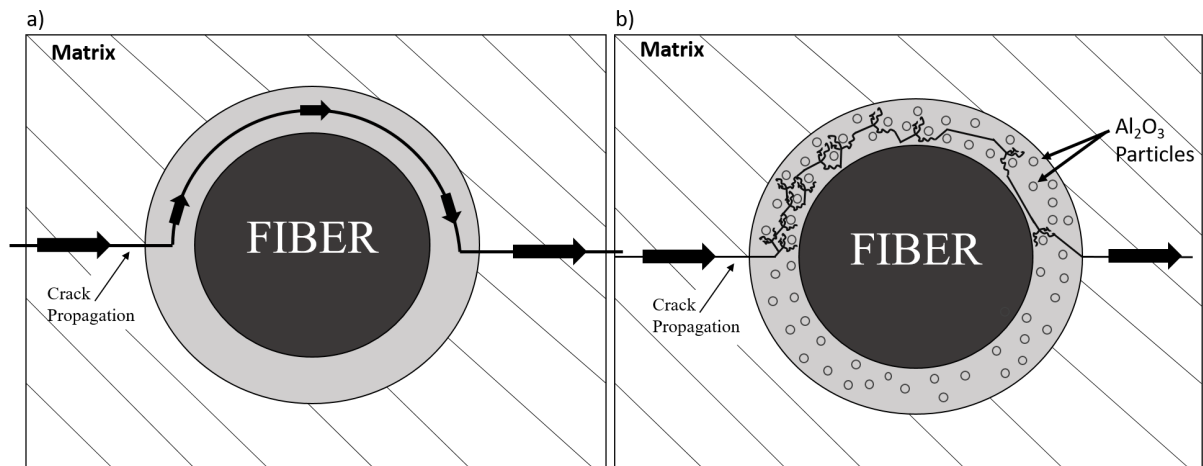


Figure 1.2: Schematic for energy dissipation mechanism through crack deflection resulting from the presence of secondary reinforcements. [2]

Inclusion of secondary particles have been show to provide for increases in microcrack stress, interlaminar shear strength, and transverse strength in fiber composites [20]. Improvements to composite flexural and interlaminar shear strength results from toughening of the matrix combined with increased roughness at the surface of the fiber-matrix interface; improvements to fracture toughness results from increased crack deflection due to the secondary reinforcement [21]. This crack deflection mechanism, shown in Figure 1.2, also results in improved tensile modulus and strength [2].

1.3 Nanoparticle Reinforcement and Agglomeration

Polymers reinforced with nanoparticles are desirable due to their unique properties and reinforcing effects. Nanoparticles offer high surface energies, due to a high surface area to volume

ratio, which greatly improves mechanical properties when compared to bulk material [22]. However, this high surface energy leads to high particle attractive forces resulting in agglomerates which decrease composite strength [19]. Polymer composites with a large presence of agglomerations have decreased polymer density and an increased polymer chain radius of gyration [23] when compared to polymer composites with the same volume fraction of well dispersed particles, which negatively impacts stiffness. In addition to weakening the polymer through adjusting the morphology, particles act as stress concentrators which further weaken mechanical properties [13]. To maximize the benefits of the incorporated nanoparticulate filler, it is necessary to optimize manufacturing parameters for the reduction of particle agglomerates. This can be done through adjusting manufacturing methods or application of components which mitigate agglomerate formation.

1.4 Silane Coupling Agents

Silane coupling agents (SCAs) are chemicals which serve to improve bonding of an organic matrix to a dissimilar material, such as an inorganic nanoparticulate filler [24, 25]. These materials have historically been applied to glass fiber reinforced polymer composites in order to increase the interfacial strength [26]; however, recent work has applied these materials to nanocomposites in order to improve particle dispersion [12]. A schematic for the mechanisms of these materials is shown in Figure 1.3. The mechanism for SCA bonding to mineral surfaces is a hydrolysis process which creates silanol groups through hydrolyzable group intermediaries

for bonding to mineral surfaces [27]. The organofunctionality of these materials is unlocked through the selection of organofunctional groups compatible with the polymer matrix. For the materials tested in this work, an epoxy-functional silane compound is selected to react with the epoxy matrix. These materials are created through either the epoxidation of unsaturated silanes or through the addition of silanes to unsaturated epoxides [28]. These epoxide groups react with epoxide groups from the matrix to form a strong covalent bond.

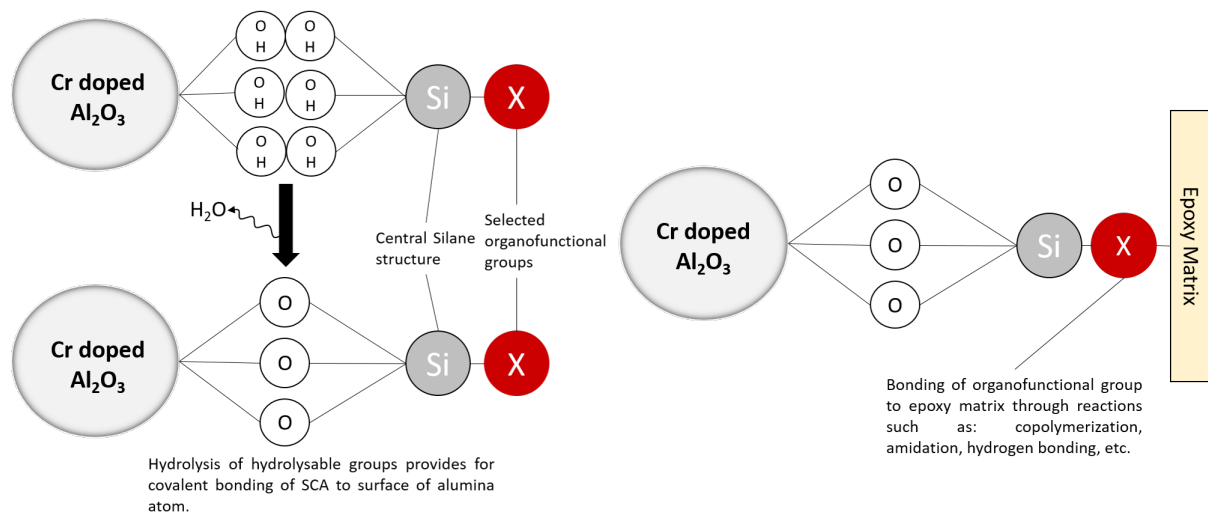


Figure 1.3: Schematic for SCA coupling processes: a) Hydrolyzable groups on alumina surface react with hydrolyzable groups on SCA to form b) covalent bond between particle surface and SCA treatment, c) bonding of SCA to organic matrix through various process.]

Reactive bonding from the particles to the matrix has the potential to reduce overall mechanical properties through prevention of particle-matrix debonding, which is a mechanism for accommodating large plastic strains, causing earlier in the composite[29]. This behavior is dependent on the stiffness of the particle-matrix interphase, and selection of proper coupling agents can mitigate this failure mechanism. In addition to facilitating mechanical reinforce-

ment, the silane coupling agent also has the potential to improve the stress sensing properties of the alumina nanoparticles within the composite through a strengthened interface. Previous work noted a maximum particle stress indicative of particle-matrix debonding, ultimately decreasing the efficacy of the PS technique at higher loads [15]. A stronger interface providing improved composite load transfer to the particles allows for accurate stress measurements at loads reaching composite failure.

A distinct class of silane coupling agents are also explored in this work. These agents are referred to as non-reactive silane coupling agents (NRSCAs), and are termed such based on the incompatibility of the organofunctional groups with the matrix [30]. As a result, covalent bonding does not occur and adhesion is dominated through weak Van der Waals interactions. While interface strength is greatly lower when compared to reactive coupling agent treatments, these treatments still provide benefits. The lack of covalent bonding is reported to provide lower polymerization stresses [30]. Improvements to particle dispersion is also reported due to a reduction in particle interactions from reduced surface tension; however this decreases particle-matrix interactions which can ultimately decrease material properties [31].

1.5 Residual Stress in Composites

Residual stress is defined as a stress that persists free of external forces or temperature gradients [32]. In composite systems this occurs when one component limits the strain of another [33], through differences in material properties such as coefficient of thermal expansions

or elastic modulus. In reinforced polymer composite systems the primary source of residual stress is due to volumetric shrinkage associated with the polymerization reaction of the matrix [34]. These stresses occur as a result of a conversion of the matrix from a viscous-plastic phase to a rigid-elastic phase [35]. This conversion is accomplished through covalent bonding of monomers for the development of a polymer network. This bonding decreases distance between the separate groups of atoms, resulting in decreased atomic spacing and decreases in overall volume. The incorporation of fibers and nanoparticles that do not accommodate this shrinkage results in residual stresses characteristic of composite materials. Applied surface treatments have an effect on the bonding of the particle to the matrix, effectively adjusting the properties of the interphase [36, 37, 38]. This is expected to result in differing residual stress states on particles with different surface treatments.

CHAPTER 2 OPTICAL SPECTROSCOPY OF Cr³⁺

The photoluminescence phenomenon occurs in alumina through the excitation of trace chromium ion impurities. Investigations into the photoluminescent emissions originated with pressure measurements in diamond anvil cells [39] and stress measurements in the thermally grown oxide layer of thermal barrier coatings [40]. Recent work has utilized this technique for the characterization of stress and dispersion behavior of composites systems with alumina reinforcement [41, 1, 42].

2.1 Photoluminescence mechanisms in alumina

The photoluminescent properties of alumina are generated from the chromium (Cr³⁺) substitutional impurities [43]. These impurities occupy sites with trigonal distortion. When these chromium impurities are excited with a laser, the material emits photons that are distributed in the shape of the characteristic R-line doublet [44]. This results from the photoluminescence phenomenon, a schematic of which is presented in Figure 2.1. Photoluminescence is defined as a non-equilibrium emission of radiation caused by a photon excitation [45]. This radiation, from the Cr³⁺ ions, occurs as a transition from the lowest energy excited state (²E_g) to the ground state (⁴A_{2g}) of the ion [46]. This transition is highly unlikely because of a spin flip requirement, being a change from a doublet to quartet energy state, which prevents a direct excitation from the ground state to the ²E_G energy level. The photoluminescence mechanism in

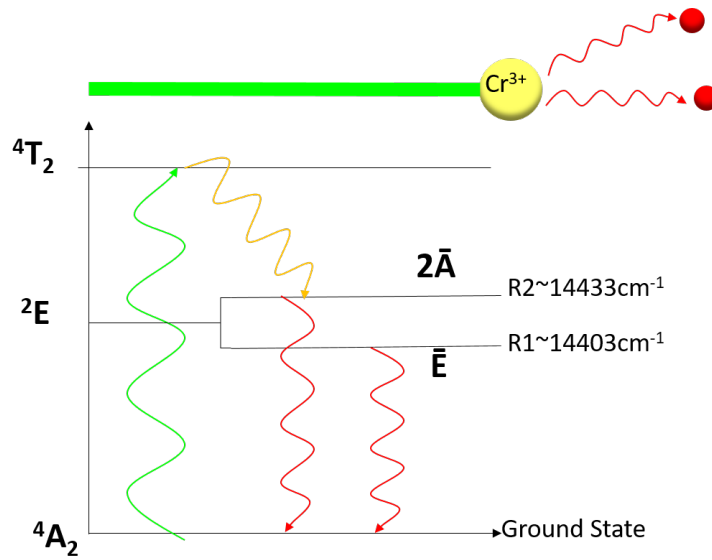


Figure 2.1: Schematic of photoluminescence mechanisms in Cr^{3+} . Initial laser impingement causes an excitation of electrons to a higher energy state. The energy state necessary for the emission of photons is reached through a nonradiative transition.

alumina therefore necessitates a nonradiative transition from higher energy quartet states (${}^4T_{1g}$ and ${}^4T_{2g}$) to the 2E_g state. The distortion present at the substitution site provides for a splitting of the 2E_g energy level into an \bar{E} and a $2\bar{A}$ energy state which results in the doublet emissions.

2.1.1 Photoluminescence Mapping

Photoluminescence measurements are a promising alternative to traditional dispersion analysis methods. These traditional methods involve processing of micrographs into binary images, where particles can be computationally resolved, allowing for characterization of agglomeration behavior [47, 48]. However, these techniques have limitations arising from micrograph

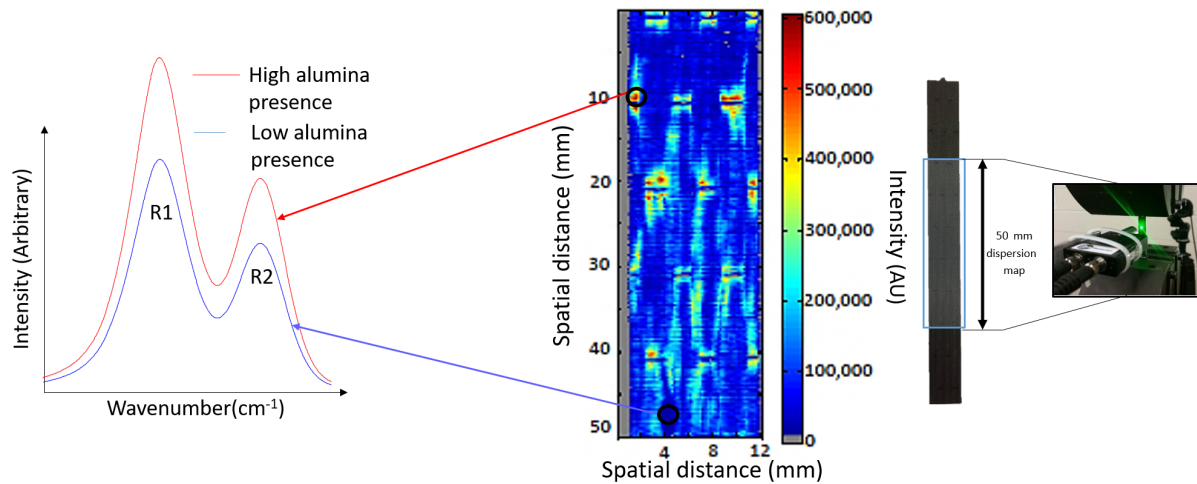


Figure 2.2: PL intensity map with data schematic showing local variations in intensity corresponding to particle dispersion [3].

quality. These occur from unclear particle boundaries in addition to the presence of hidden particles [49] not clearly resolved. As such, for the large scale characterization of dispersion behavior it is necessary to utilize a different technique.

Photoluminescence spectroscopy was developed in work preceding this for the characterization of dispersion in polymer nanocomposites [14]. With this technique, the intensity of photoluminescence emissions are compared across a scanning regions. Locations with higher intensity emissions have higher alumina concentrations. Significant deviations in surface intensity distributions are indicative of poor particle dispersion. This method was utilized in order to characterize dispersion in hybrid carbon fiber composites [3], and is further developed in order to provide for quantitative analysis of intensity distributions for determination of optimal dispersion behavior. An example of a photoluminescent map with a schematic of local data is presented in Figure 2.2.

2.2 Piezospectroscopy

The doublet emissions of Cr^{3+} (Figure 2.2) are known to have energies dependent on the applied stress state [50]. This sensitivity arises from changes in ligand length from applied stress, resulting in field induced changes to the energy states of the chromium ions [51]. The photoluminescence of chromium doped alumina has been extensively studied [44, 52, 53] and found to follow the piezospectroscopic relationship which is a tensorial relation between doublet peak shift and applied stress, presented in Equation 2.1 [40]:

$$\Delta\nu = \Pi_{ij}\sigma_{ij} \quad (2.1)$$

where $\Delta\nu$ is doublet peakshift, Π_{ij} is the experimentally measured PS coefficient tensor [54], and σ_{ij} is the stress tensor. In the case of polycrystalline alumina this equation has been adjusted in order to form a relationship between the hydrostatic stress and wavenumber shift and is presented in equation 2.2 [50]:

$$\Delta\nu = \frac{1}{3}\Pi_{ii}\sigma_{ii} \quad (2.2)$$

where Π_{ii} is the trace of the experimentally measured PS coefficient tensor and $\frac{1}{3}\sigma_{ii}$ is the hydrostatic stress. Of the two peaks, the higher intensity one (denoted R1 having a zero stress peak position of 14403 cm^{-1} [55]) is generally selected for monitoring due to increased accuracy from better signal intensity. The polycrystalline nature of the embedded nanoparticles provides for additional stress dependence. The peak width has been related to the second

principal invariant of the stress deviator tensor [50]. The tensorial relationship is shown in equation 2.3.

$$\begin{aligned} \langle \Delta\nu^2 \rangle = & \frac{4}{15} [(\Pi_{22} - \Pi_{11})^2 + (\Pi_{33} - \Pi_{11})^2 - (\Pi_{22} - \Pi_{11})(\Pi_{33} - \Pi_{11})] \\ & \times \left[\frac{1}{3} (\sigma_{11}^2 + \sigma_{22}^2 + \sigma_{33}^2 - \sigma_{11}\sigma_{22} - \sigma_{22}\sigma_{33} - \sigma_{33}\sigma_{11}) + (\sigma_{12}^2 + \sigma_{23}^2 + \sigma_{31}^2) \right] \end{aligned} \quad (2.3)$$

The R1 peak is again selected for monitoring. The broadness of the peak is defined to be the width of the peak at half of the maximum intensity. This value can then be tracked with applied loading allowing for measurement of deviatoric stresses.

2.2.1 Piezospectroscopic Mapping

This technique can similarly be applied to the mapping of stress across a sample surface. Work preceeding this has utilized digital image correlation and piezospectroscopy for the analysis of carbon fiber samples coated with a non-reinforcing stress sensing coating undergoing open hole tension tests [42]. It was found that this technique provided for earlier crack detection when compared to DIC. This technique can provide for unique measurements of internal composite stresses in different local regions. Embedding of nanoparticles within the carbon fiber composite allows for measurements of load transfer from matrix to particles, which can be extrapolated to provide overall composite load transfer behavior [1]. This stress sensitivity occurs alongside the mechanical property reinforcement through nanoparticle reinforcement. For the work presented, piezospectroscopy is utilized in order to characterize residual stress result-

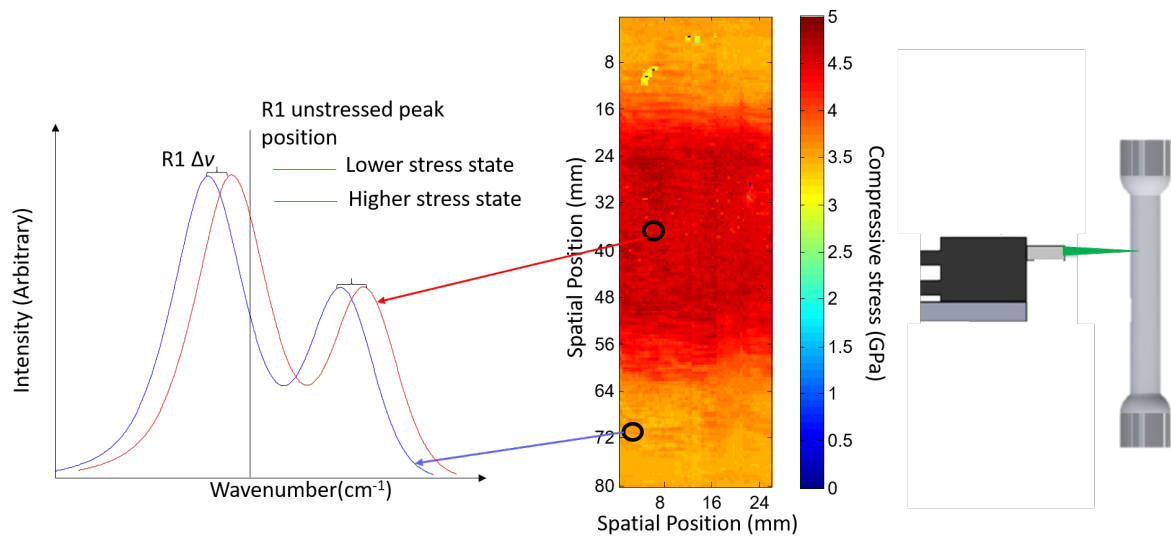


Figure 2.3: PL peak shift map with data schematic showing local variations in wavenumber corresponding to local stress state. Values can be converted to stress through application of the PS equation [4].

ing from sample manufacturing in the embedded nanoparticles. A peakshift map is presented in Figure 2.3 with schematics of shifted R-line corresponding to stress variations experienced across the sample surface.

CHAPTER 3 EXPERIMENTAL METHODS

Individual photoluminescence measurements provide for both local intensity and stress, accomplished through collections with spectroscopy systems. These systems are described along with experimentation parameters. Sample manufacturing steps for the creation of hybrid carbon fiber composites with stress sensing capabilities are also presented. In addition, there will be a description of processes for fitting the R-lines, necessary in order to correctly track peak position and peak width.

3.1 Photoluminescence Collections

For the collection and processing of photoluminescent emissions it is necessary to utilize several systems. For this work, photoluminescent emissions were captured using a portable piezospectroscopy system and a confocal Raman system. The method for processing and fitting the photoluminescent emissions are also presented in this section.

3.1.1 Portable Piezospectroscopy System

The system utilized for collection of large area photoluminescent emissions combined several different optical systems. Figure 3.1 outlines these components combined into a Portable Piezospectroscopy System [56]. This system incorporates a Princeton Instrument Pixis 100

charged coupled device, Acton SP2150 spectrometer with a 1200 lines/mm grating, and an InPhotonics Inc. RPB Raman Probe. The laser used outputs approximately 13mW from the probe. Utilized alongside the optical collection system is an x-y-z translation stage, upon which the probe is placed. This system allows for high spatial resolution photoluminescence collections across surfaces. A schematic of this equipment is presented in Figure 3.1.

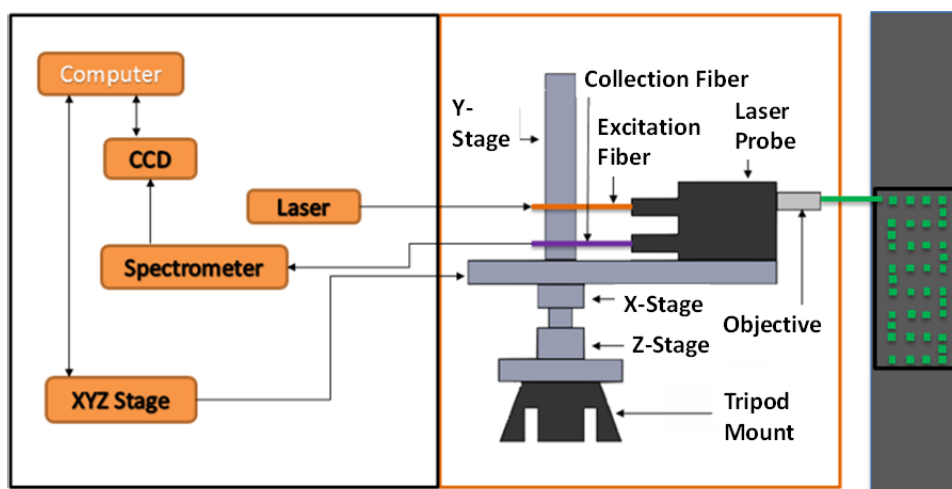


Figure 3.1: Schematic for equipment used to collect and track photoluminescence emissions from aluminum oxide.

3.1.1.1 Experimental Parameters for Photoluminescence Measurements with Portable System

The spatial resolution of the PL measurements was set to $200 \mu\text{m}$ [18]. For the intensity measurements 10,000 points were taken in a central $10 \times 40 \text{ mm}$ zone. Collection parameters had to be altered between samples in order to maintain the emissions at an intensity below the CCD

saturation intensity and to maintain the signal to noise ratio above a minimum threshold. To allow for intensity comparisons between samples with different collection parameters, intensities were normalized to the laser fluence. The equation for laser fluence is presented in equation 3.1 [57]. This both allowed for comparisons between samples and for highlighting differences between faces of a sample.

$$Fluence = \frac{LaserPower \cdot Collectiontime}{Laserspotsize} \quad (3.1)$$

3.1.2 High Resolution Investigations

A separate emissions collection system was utilized for higher resolution investigations at the UCF Nanoscience Technology Center. The system utilized was the WITec 300 RA confocal Raman system [5]. In this case, the spectrometer used had an 1800 lines/mm grating. Photoluminescence maps created with this system were taken with a 50x microscope objective which results in a 200 nm spatial resolution. The resolution of this system is several orders of magnitude higher than of the portable system and approaches the size of the nanoparticles. This allows for the system to resolve variations in stress between individual particles. These differences are highlighted in Figure 3.2. Micrograph images of the scanning area provide morphological information in combination with the photoluminescent patterns for the understanding of material structures on particle dispersion. A 1.5 mW laser power was used as it provided sufficient excitation without damaging the sample.

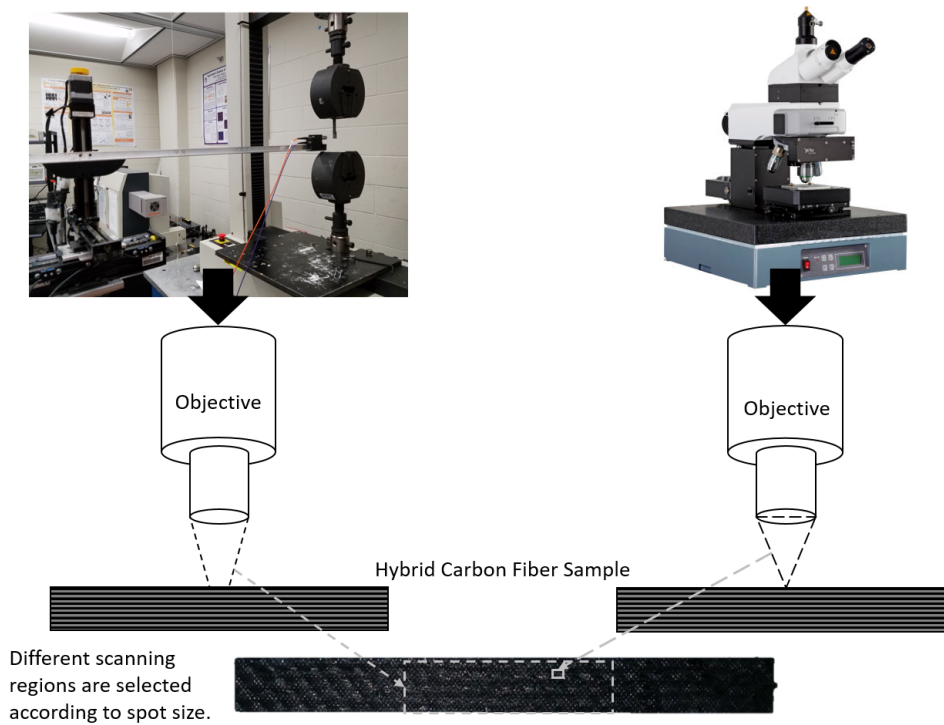


Figure 3.2: Different laser spot sizes allow for different spatial resolution for the collection of intensity and piezospectroscopic data [5].

3.1.2.1 Experimental Parameters for High Resolution Measurements

For these investigations, only the 12 wt% samples are examined. It was found that lower particle loadings had PL emissions with low signal to noise ratios. Every treatment type was investigated in order to isolate differences in behavior that arise from the different particle bonding mechanisms imparted by the different surface treatments. Furthermore, 3 randomly selected points were investigated in order to account for statistical variation. The scanning regions were selected to include 2-3 fibers and as such dimensions were altered between scans; however, areas scanned were generally maintained near $100 \mu\text{m}^2$. Collection times were set to

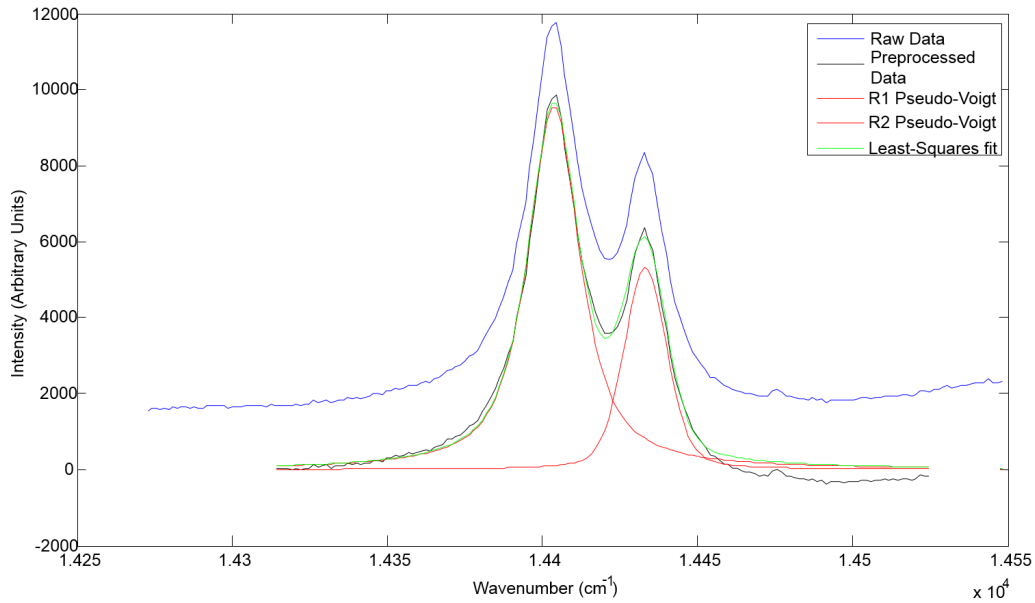


Figure 3.3: Transformation of raw spectral data to individual pseudo-Voigt functions and fitted doublet [6].

1 second in order to ensure high signal to noise ratios. The scanning was conducted in a Raster pattern, with one collection every 200 nm.

3.1.3 R-line processing and analysis

A MATLAB® program, developed by Freihofer [58], based on a least squares fitting function is utilized for processing. Figure 3.3 shows the transformation from the raw data to the final fitted data that is used to monitor the position of the R1-R2 peaks in order to determine stress.

Preprocessing steps, developed by Raghavan [59] for a genetic algorithm, are required in order to prepare the least squares algorithm for doublet fitting. The first process performed is

the sectioning of the data. The frequencies included in the raw data generally contain excess information that can distort the least squares fitting process. As a result, points are selected where the derivative of the R-line tails is equal to zero. Data outside of this range is removed, leaving just the desired R-line spectrum. The bounds are also used to define the baseline. This baseline intensity can then be removed through linear fitting. The result of the final step is the determination of the initial guess for the R1 and R2 pseudo-Voigt functions. Using an estimation of the fitted peaks from the raw data, the initial guesses for the full width at half maximum (FWHM), peak position, area under the curve, and Gaussian ratio for both peaks of the doublet are determined.

The pseudo-Voigt functions used to fit both peaks of the doublet are a convolution of Gaussian and Lorentzian line-shapes and have been shown to be an accurate function for the fitting of symmetric peaks [60]. This function assumes that the line-widths of Gaussian and Lorentzian components are equal and is represented as follows [58]:

$$\Phi(\nu) = 2A[\Phi_G(\nu) + \Phi_L(\nu)] \quad (3.2)$$

The $\Phi(\nu)$ term is the combined function, the $\Phi_G(\nu)$ term is the Gaussian function, and the $\Phi_L(\nu)$ term, is the Lorentzian function, and A is the integrated intensity under the spectral function. The Gaussian and Lorentzians functions are shown in Equations 3.3 and 3.4 respectively [58].

$$\Phi_G(\nu) = \frac{GR}{W} \sqrt{\frac{\ln 2}{\pi}} \exp\left(-4 \ln 2 \left(\frac{\nu - C}{W}\right)^2\right) \quad (3.3)$$

$$\Phi_L(\nu) = \frac{LR}{\pi W [1 + 4(\frac{\nu - C}{W})^2]} \quad (3.4)$$

For both Gaussian and Lorentzian functions, W is the FWHM, A is the area under the curve, and C is the peak position. The GR term in Equation 3.3 represents the Gauss Ratio, which represents the contribution of the Gaussian lineshape to the pseudo-Voigt function, and is related to the Lorenz Ratio (LR) by $GR = 1 - LR$. The $R1$ and $R2$ pseudo-Voigts are combined in Equation 3.5 to represent the R-line doublet function which contains 8 variables (4 variables for each pseudo-Voigt) [58]. Relationships between $R1$ and $R2$ variables based on applied load exist and are used to set the upper and lower bounds in order to tie the physical phenomena with the curve fitting algorithm [59, 61].

$$\Phi_{doublet}(\nu) = \Phi_{R1}(\nu) + \Phi_{R2}(\nu) \quad (3.5)$$

3.2 Sample Manufacturing

The hybrid carbon fiber samples investigated in this work were manufactured by collaborators at Imperial College London and are a combination of three components: being the alumina nanoparticles, carbon fibers, and polymer matrix. These samples were manufactured through a technique known as resin infusion under flexible tooling (RIFT) [62]. This technique utilizes a

vacuum-assisted resin transfer moulding method in order to infuse stacked carbon fiber sheets with a resin modified with the nanoparticles. This procedure generally provides for decreased void presence in addition to allowing for higher fiber volume fraction capabilities. The curing of these samples were conducted following bulk polymer procedures. Three particle loadings were explored in this work and three different types of surface treatment were utilized in sample manufacturing. All combination of manufacturing parameters explored are presented in Table 3.1.

Table 3.1: All combination of manufacturing parameters for the creation of 9 unique samples

	6 wt%	9 wt%	12 wt%
Untreated	o	o	o
RSCA treated	o	o	o
NRSCA treated	o	o	o

3.2.1 Nanoparticle/Polymer Mixture

The nanoparticles chosen were α -alumina nanoparticles provided by Inframat® Advanced Materials™, USA. These particles have a purity of 99.85%, average grain size of 40 nm, and average particle size of 150 nm, and a multi-point surface area of approximately 10 m²/g [63]. The polymer matrix used consists of a resin and curing agent, available commercially as Epikote 862 and Epikure 3402, with the resin being Bisphenol F and epichlorohydrin based

and the curing agent being aromatic di-amine based [64]. These materials were selected for their properties which reduce filler settling and clustering [64]. Particles were added to the resin prior to the infusion process. In order to reduce agglomerations, a sonication process was utilized in order to improve homogeneity of the resin [65]. After sonication, the resin and curing agent were mixed in a 26.4:100 stoichiometric ratio. The resulting solution was then mechanically stirred and degassed in order to remove pockets of trapped air. For samples with nanoparticle functionalizations, the coupling agent is introduced into the resin. The coupling agents used were trimethoxysilane (a reactive SCA) and trimethoxysilyl (a nonreactive SCA). As previously mentioned, the SCAs react chemically with the hydroxyl groups on the surface of the nanoparticles through a hydrolysis reaction to form a covalent bond. This results in a strong covalent bond between the coupling agent and the nanoparticles. Upon the completion of these processing steps, the resin is prepared for infusion.

3.2.2 Infusion of Carbon Fibers

The carbon fiber weave utilized for the creation of these composites is the unidirectional UT-C400 with carbon 12k fibre type manufactured by Marineware [66]. Eight plies of carbon fiber were stacked and resin infusion was conducted parallel to direction of the fibers. This process is shown in Figure 3.4. Upon curing, these steps provide for a composite sheet that is 3 mm thick. The curing cycle was conducted following manufacturer recommendations, being 4 hours at 120°C followed by 4 hours at 170°C, with a ramp rate of 2°C/minute. This curing cycle was

previously found to be optimal for minimizing particle agglomeration and sedimentation [64]. It is during this curing process where any residual stresses are introduced. Volumetric shrinkage of polymers occurs during curing and the raised temperature of the process imparts a small strain at room temperature due to the coefficient of thermal expansion mismatch.

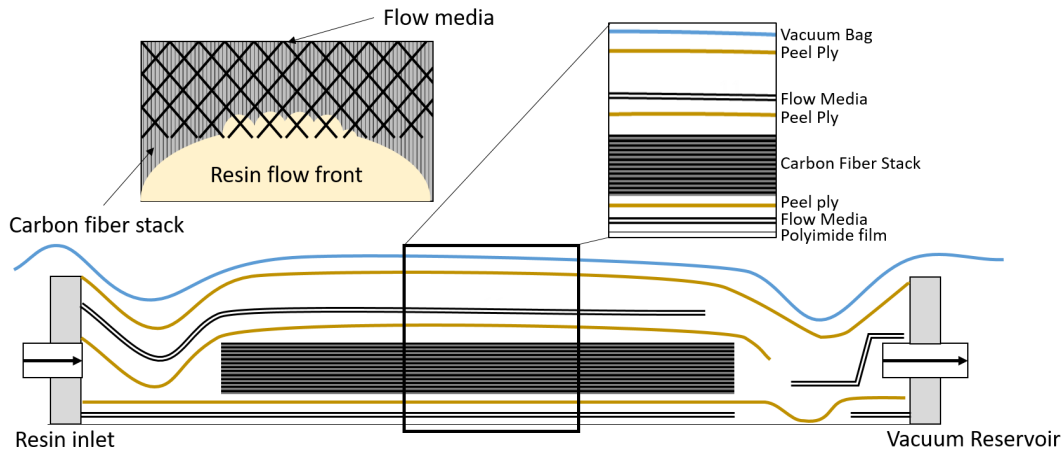


Figure 3.4: Schematic outlining manufacturing of hybrid carbon fiber composite sheets through the resin infusion under flexible tooling (RIFT) process. A schematic outlining resin guidance with flow media is also presented.

3.2.3 Sample Design

Upon curing, samples were machined from the bulk composite material for analysis. Waterjet cutting was utilized due to the technique's low cutting force and lack of thermal distortion, which is associated with other machining techniques [67]. The sample dimensions were selected as 100x10x3 mm. A sample along with a schematic are presented in Figure 3.5. The

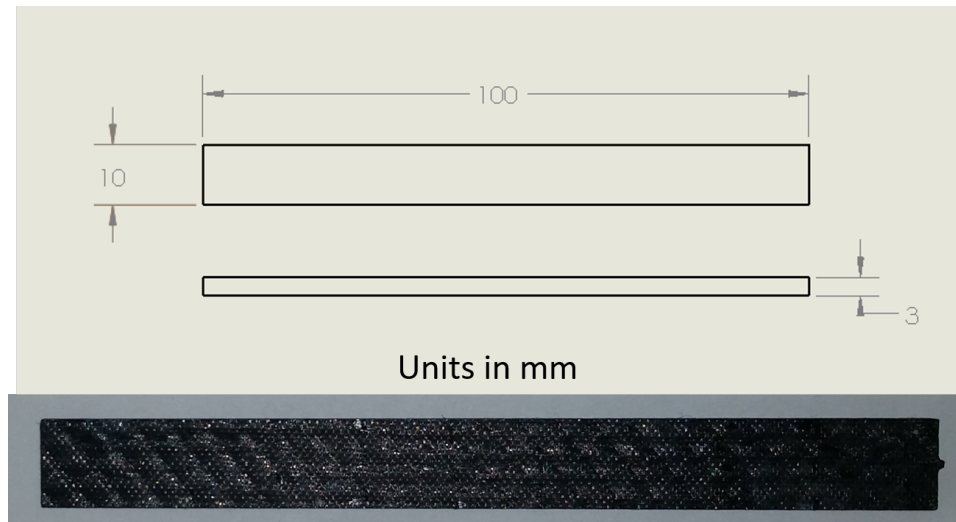


Figure 3.5: a) Schematic of design with labeled dimensions and b) image of sample tested

sample surface is seen to not be completely flat and instead is patterned with regularly spaced hills and troughs. This patterning is believed to be an artifact of the flow media used during infusion of resin. Effects of this artifact on particle dispersion is discussed in future sections.

CHAPTER 4 PARTICLE DISPERSION ANALYSIS

Particle dispersion measurements were carried out in order to compare dispersion behavior of samples with differing manufacturing parameters. These results are presented as intensity contour maps, in which higher intensity values correspond to higher particle concentrations. These results are then converted to intensity distribution histograms which more clearly show dispersion behavior. The variance to mean ratio is then utilized as a quantitative value which can directly compare degrees of dispersion between samples. Finally a sedimentation coefficient representing the degree of homogeneity through sample thickness is discussed.

4.1 Qualitative Analysis of Weight Percentage Effects on Particle Dispersion

Prior to the presentation of the dispersion contour maps, it is necessary to understand what information can be gleaned. For each surface treatment, the effects of weight percentage on the particle dispersion can be qualitatively analyzed. This is done by viewing the inhomogeneity of pixel values across each intensity contour map. Samples that have large intensity variations in different regions have poor particle dispersion. This is seen as regions of bright red pixels surrounded by regions of dark blue pixels. Sedimentation, which is the settling of particles to one face of the sample during manufacturing, can also be quantitatively analyzed. Samples with large amounts of sedimentation are characterized by contour maps in which one side has a much higher average intensity than the other. Grey pixels in these maps represent points

with emissions that are of extremely poor signal quality and were not analyzed as a result. As previously mentioned, the presented intensities are normalized to the laser fluence used during collection. Two sets of samples for each nanoparticle loading and surface treatment were tested; however, only one set of contour maps are presented for each as both sets share similar behavior.

4.1.1 Untreated Dispersion Behavior with Increasing Weight Percentage

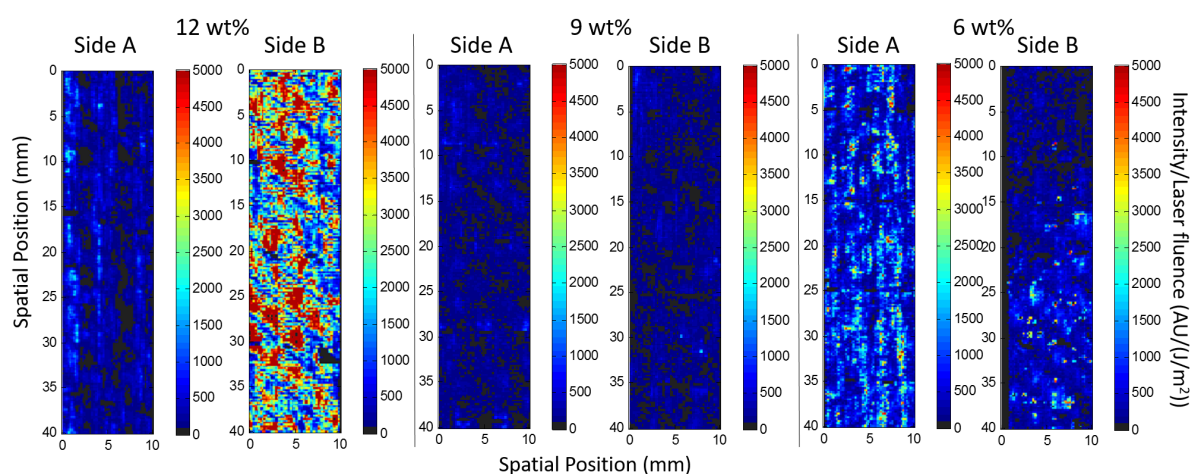


Figure 4.1: Dispersion maps for untreated sample showing increased particle agglomeration with highest particle loading.

The results for one set of the untreated samples is shown in Figure 4.1. Qualitative analysis shows that the 12 wt% side B sample has the most inhomogeneous contour map. This is seen from the large intensity variations which dominate the surface. The contour maps for the 9 wt% sample are both very uniform in value and are examples of samples which showcase well

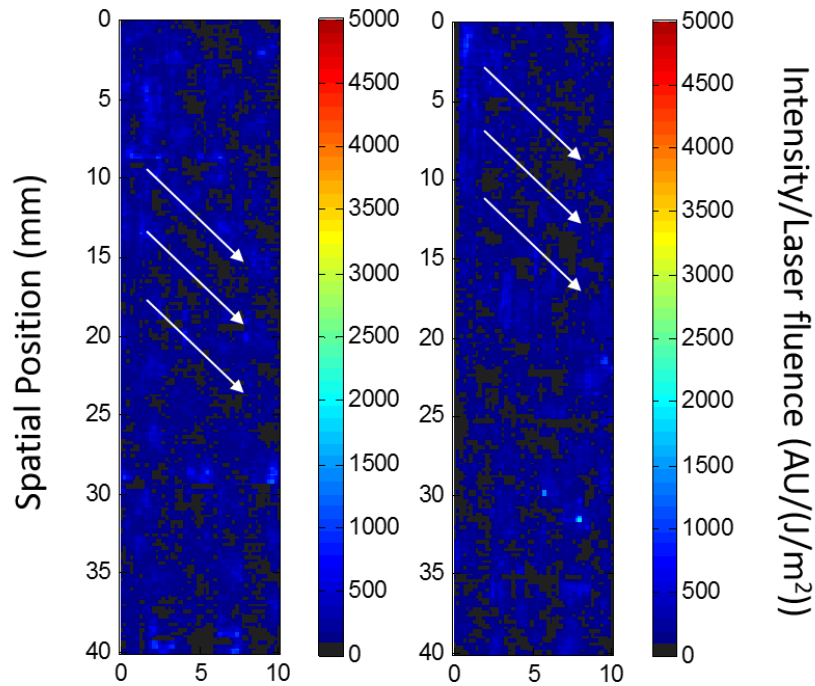


Figure 4.2: Low concentration lines in 9 wt% untreated samples where the white arrows indicate direction.

dispersed behavior. It is noted that the 9 wt% sample has definitive examples of dispersion patterning. This patterning is highlighted in Figure 4.2. This is seen in other samples and occurs as a result of the flow media used. The flow media is a sheet used in the RIFT process to help distribute the resin through capillary action [68], seen in Figure 3.4. The flow media used for the creation of the analyzed samples had a crisscross pattern, and points which impinged on the sample have lower amounts of resin, and as such lower amounts of particles.

The contour maps of the 6 wt% sample are both seen to have worsened dispersion when compared to the 9 wt% sample and is contrary to the expectation that increasing weight percentage of particles leads to worsening of dispersion. This behavior may result from a combination

of the resin flow properties with the manufacturing technique. Literature reports that the level of particle loading has an effect on resin flow properties [69]. These properties [70] alongside the structure of the flow media [68] can impact the infusion rate, which ultimately affects particle dispersion. Future investigations into resin flow properties with differing particle loadings will be necessary to discern this behavior.

Analysis of differences between the sample faces at each weight percentage allows for a qualitative analysis of loading effects on sedimentation. It is seen that sedimentation is less present in the 9 wt% sample than the 6 and 12 wt% samples. This is seen from the large overall difference in intensities between faces in the 6 and 12 wt% sample. The 9 wt% sample is said to have lessened sedimentation due to the extremely similar overall intensities on both faces. This is indicative of a more consistent distribution of particles through thickness when compared to the other weight percentages.

4.1.2 Surface Treatment Effects on Dispersion Behavior

The dispersion maps for the samples treated with RSCA are presented in Figure 4.3. The RSCA treated samples have a much more consistent dispersion behavior between sides and weight percentages. The previously mentioned patterning is also more present in these samples, with clear low concentration lines in every contour map. With this surface treatment, the dispersion of particles tends to worsen with increasing loading. The 6 wt% particle loading provides the optimum dispersion of particles among all RSCA treated samples. Comparisons of side

A and B for all weight percentages show similar overall intensities, indicative of lessened sedimentation when compared to the untreated sample.

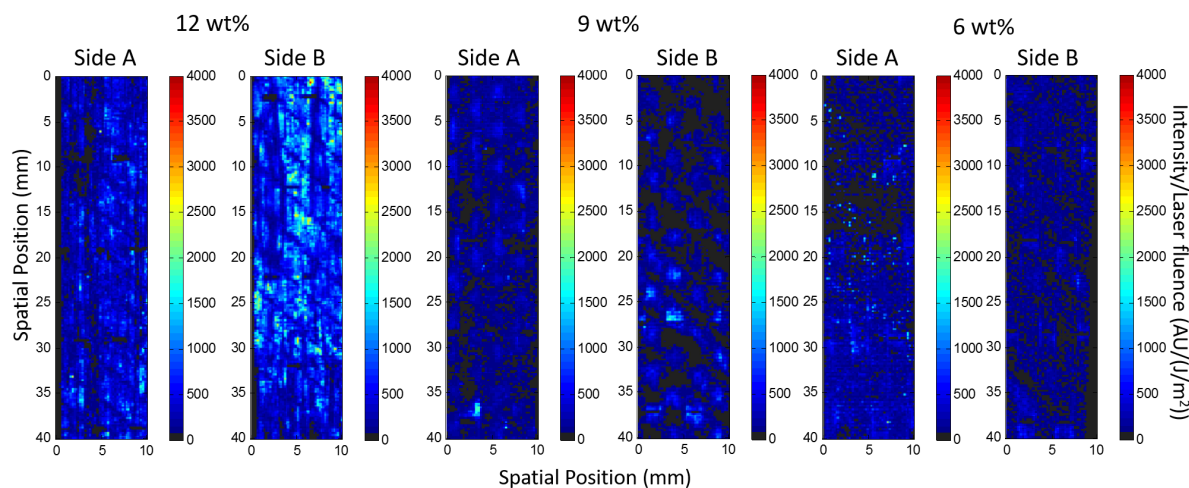


Figure 4.3: RSCA treated sample dispersion maps showcasing consistent intensities across surfaces with presence of small agglomerations.

The NRSCA dispersion maps are presented in Figure 4.4. Weight percentages affects the NRSCA treated sample dispersion behavior in similar ways to the RSCA treated samples. There is an increase in high concentration spots with increasing weight percentage of particles. In this case, it is difficult to discern the optimally dispersed sample between the 6 and 9 wt% particle loadings. Sedimentation is also seen to be mitigated by the NRSCA treatment. While samples with higher particle loadings experience more particle clustering, these spots occur on both faces of the sample as seen in the 12 wt% sample. Exact comparisons of dispersion and sedimentation are not possible simply through qualitative analysis. Quantitative analysis of dispersion and sedimentation will be discussed in the following sections.

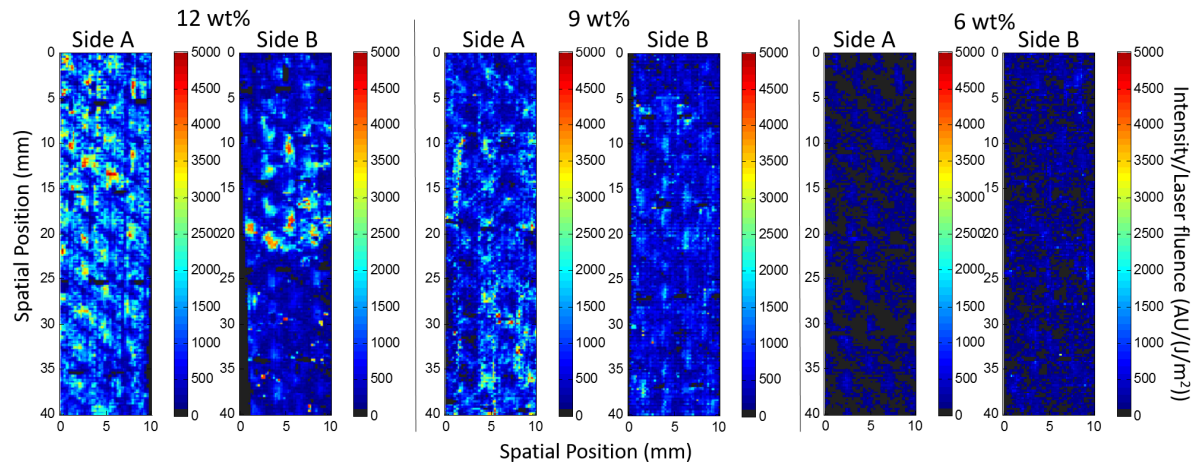


Figure 4.4: Dispersion maps for NRSCA treated samples. Large agglomeration behavior is present in 9 and 12 wt% samples.

4.2 Quantitative Analysis of Dispersion and Sedimentation

It is necessary to describe dispersion and sedimentation in terms of numeric values in order to directly compare manufacturing parameters. This numeric characterization will also allow for the future development of constitutive equations which can calculate mechanical responses based on composite particle dispersion in future work. The contour maps are first converted into intensity distributions which provide a basis for statistical analysis. These distributions are then analyzed to provide for a comparative measurement of dispersion. Finally, sedimentation coefficients for each sample are produced.

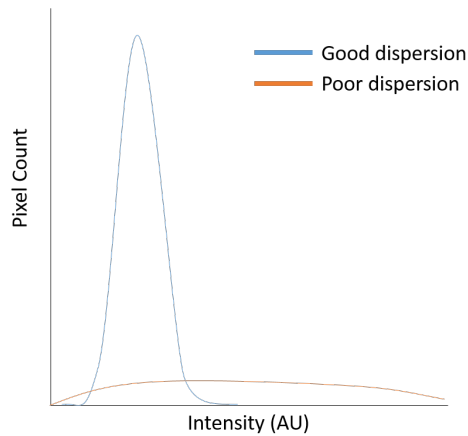


Figure 4.5: Schematic outlining intensity distributions for well dispersed and poorly dispersed samples [3].

4.2.1 Conversion of contour plots to intensity distributions

The histograms constructed from the contour maps showcase the distribution of intensities across the surface of the samples by plotting the counts of pixels at a certain intensity versus the full range of intensities. Well dispersed samples are characterized by intensity distributions with lower widths and higher counts at the mean intensity. A poor dispersion is instead characterized by an intensity distribution with a large variance, as a result of a larger spread in intensity values due to particle clustering. A schematic outlining this difference is presented in Figure 4.5. The intensity distributions for all samples are shown in Figure 4.6. Both sides of each sample are plotted with the same line type in order to show dispersion differences in each side which primarily result from sedimentation.

The first analysis presented will discuss weight percentage effects on particle dispersion. Increasing weight percentage of particles is seen to result in increasingly wider distributions,

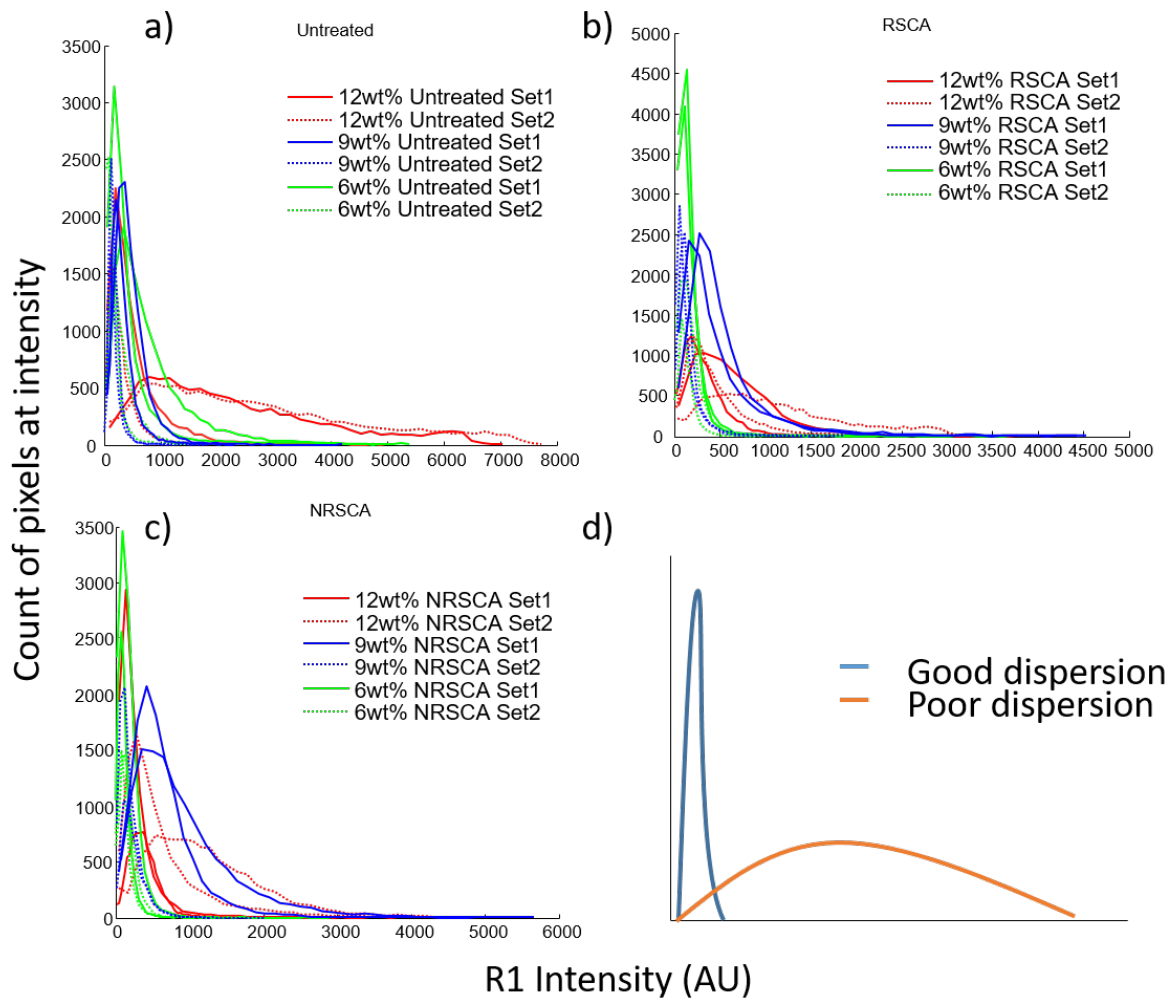


Figure 4.6: Intensity distributions for a) Untreated samples, b) RSCA treated samples, c) NRSCA treated samples, and d) a schematic outlining good dispersion and poor dispersion.

indicative of worsening dispersion. This is most evident in Figure 4.6a, where the 12 wt% untreated sample distribution is much wider than the distributions for the 6 and 9 wt% samples. This broadening is seen to be mitigated with the addition of the surface treatment.

For reviewing these distributions it is imperative to review both distributions to compare behavior between sample faces. It is necessary for nanoparticles to be optimally dispersed on both faces of each sample in order to provide for a more homogeneous distribution of particles through thickness. This difference in distribution widths, characteristic of sedimentation, is seen in every 12 wt% sample regardless of surface treatment. The magnitude of the width difference is largest in the untreated sample. One face of the 12 wt% untreated sample has a distribution which closely follows the 6 wt% distributions while the other face is much wider. This difference in width is of a lower magnitude in the treated samples.

Quantitative analysis of these histograms leads to two main conclusions. The first conclusion regarding particle dispersion is, as previously stated, that the application of surface treatments on the particles mitigates the higher particle attractive forces that occur in composites with higher particle loadings. Particles still tend to cluster in high concentration zones with the surface treatments, as seen in the contour maps; however, the associated distribution broadening is smaller than the broadening associated with the untreated sample. The second conclusion is that the degree of sedimentation is also lessened with the application of the surface treatment. Distributions of both faces are seen to follow each other more closely with the treatment than without the treatment.

4.2.2 Dispersion Characterization through Variance to Mean Ratio

While quantitative comparison between samples can be conducted for each treatment type, it is necessary to utilize a dispersion coefficient which is independent of particle intensity for comparison between treatments. The treated samples tend to experience increasingly lower emission signal quality with lower nanoparticle loading. This can result from a variety of factors, including lowered average presence of particles as well as the formation of an interphase around the particles which may dampen photoluminescent emissions; and as a result, intensities between samples do not necessarily correlate to the same concentrations. This renders a direct comparison of distribution widths useless. In order to quantitatively compare between the samples with different emission behaviors, the variance to mean ratio is utilized as a measurement of particle dispersion.

The variance to mean ratio (VMR) is a statistical value which is used in order to characterize the spread of data around the mean of the distribution [71]. This value was originally utilized for the characterization of the dispersion of botanical species in spatial regions [72] and is calculated by dividing the variance of the data by the mean. This is shown in equation 4.1:

$$VMR = \frac{\sigma^2}{\mu} \quad (4.1)$$

where σ^2 is the variance and μ is the mean of the distribution. The value of the measurement is on a scale from 0 to infinity, where 0 is a perfectly dispersed specimen, 1 is a specimen with a random dispersion (defined by the Poisson's function), and values greater than 1 have dispersion characterized by clustering. The standard for the random dispersion of values is

presented in Figure 4.7 with two of the previously presented histograms. Comparisons of distributions by the VMR allows for determination of optimal manufacturing parameters.

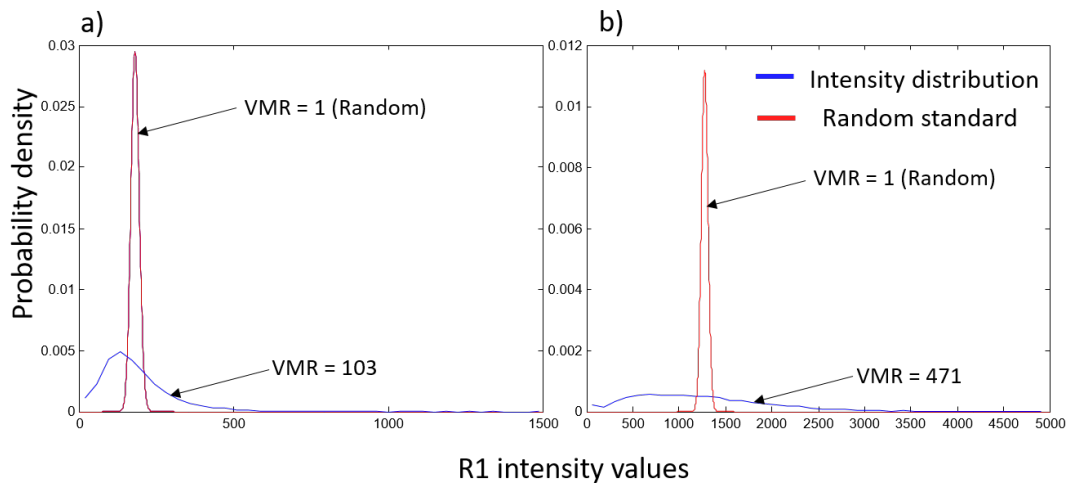


Figure 4.7: Two examples of of previously presented intensity distribution histograms plotted against the standard random distribution of data at the same mean, which is represented by the Poisson's distribution. Plot a) is seen to have a more random distribution than plot b) and a lower VMR.

The variance to mean ratio is utilized in this work as opposed to other measurements of dispersion as a result of the nature of the PL measurement technique. Other quantities have been established in literature to describe dispersion. These values are generally dependent on microstructural analysis and generate comparable values of dispersion based on factors such as relative particle size [73, 74], comparisons of distances between features [75], and others [76, 77, 78]. While these values are generally robust and provide for very good characterization of dispersion, they cannot be applied to the intensity distributions presented. The PL measurement technique is not capable of resolving microstructural features. Instead this technique provides

relative particle concentrations within the measurement zone through the emission intensities. As a result, analysis of dispersion with this technique is seen to be more similar to quadrat methods [79]. These methods measure concentration of a dispersed specimen, in this case the nanoparticles, in a spatial grid pattern. The count of specimens in each grid is then plotted as a distribution similar to the previously developed intensity histograms. The variance to mean ratio of this distribution is then calculated as a simplistic and robust measure of dispersion. There are limitations that exist with utilizing the VMR for dispersion analysis arising from a dependence on the grid size[80]. However, the PL technique measures concentration of nanoparticles, through the intensities, in a grid pattern where each grid is defined by the spatial resolution of the measurement technique. The spatial resolution is orders of magnitude higher than the specimen size (microns to nanometers) and ten thousand total grids are examined which serves to remove the issues arising from under-sampling. Furthermore, all samples were collected with the same spatial parameters which reduces the bias that may be associated with grid size. This bias can also be ignored because the calculated variance to mean ratio is not utilized to characterize which samples are sufficiently dispersed, but instead serve only to characterize which samples are better dispersed.

Two graphs for VMR are presented in Figure 4.8 which are separated by set number. Samples are arbitrarily selected to be set 1 and 2; and so the differences in behavior highlight the variability of the manufacturing technique. Optimal dispersion of particles results in a VMR of 0, and so the lowest values are desired. The lines plotted represent the average VMR for all similarly treated samples in a set. This allows for the analysis of the effects of surface treatment

on the dispersion of particles for all particle loadings. Each point is the average VMR between both faces of the sample, and the range is represented by the brackets on each point.

Normalized variance show less dispersion variation with treatments

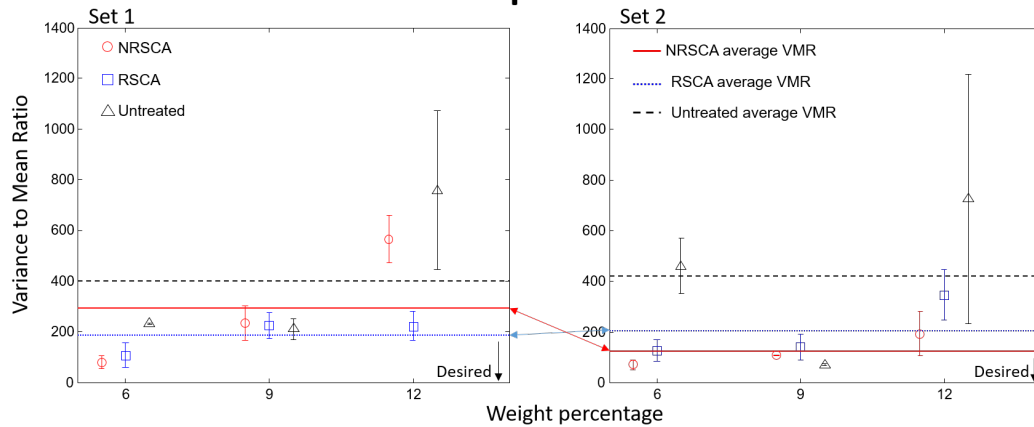


Figure 4.8: VMR plotted for both sets of each sample. The lines represent the overall average VMR in order to highlight the optimal overall dispersion and variations in dispersion between volume fractions. The RSCA treatment provides the most consistent improvements to dispersion and is found to be the most independent of manufacturing parameters

In both cases the overall average VMR is lowered with the presence of surface treatments. This results from the previously described mechanisms which counterbalance particle attractive forces reducing the drive for particle clustering. Inspecting the variation of values from the average VMR shows that the untreated samples tend to have dispersion behavior that is more dependent on particle loading than the treated samples. Furthermore, in both sets of samples the RSCA is seen to be the most particle loading independent. In both cases, the overall average VMR is maintained very close to 200 with low variations away from the average for each individual data point. The difference in average VMR in the NRSCA treated samples shows

an increased sensitivity to manufacturing conditions. This is proposed to result from the lack of covalent bonding mechanisms in the NRSCA. This surface treatment only serves to reduce the surface energy of the particles. As such, the clustering behavior is still dependent on the magnitude of particle attractive forces; which arises from the initial dispersion of particles from the sonication process and how the particles are distributed in the resin during the infusion processes. This results in greater variability, when compared to the RSCA sample which can lock the initial dispersion from the sonication process in place and maintain it during the infusion process.

4.2.3 Sedimentation Analysis

Dispersion behavior across each sample face must also be compared to the opposite sample face in order to ensure a homogeneous distribution of particles throughout the thickness of the sample. The difference in particle concentration between sides is referred to as sedimentation, and this behavior can be quantified through the comparison of surface integrals for both faces of the sample. This method for sedimentation characterization was developed by Hanhan [3] for similar hybrid carbon fiber composites. This work showed that the surface integral of PL contour maps can be approximated as the summation of the intensity values for each pixel (R_n) multiplied by the area of the map (XY), which is shown in Equation 4.2.

$$I = XY \sum_{n=1}^N R_n \quad (4.2)$$

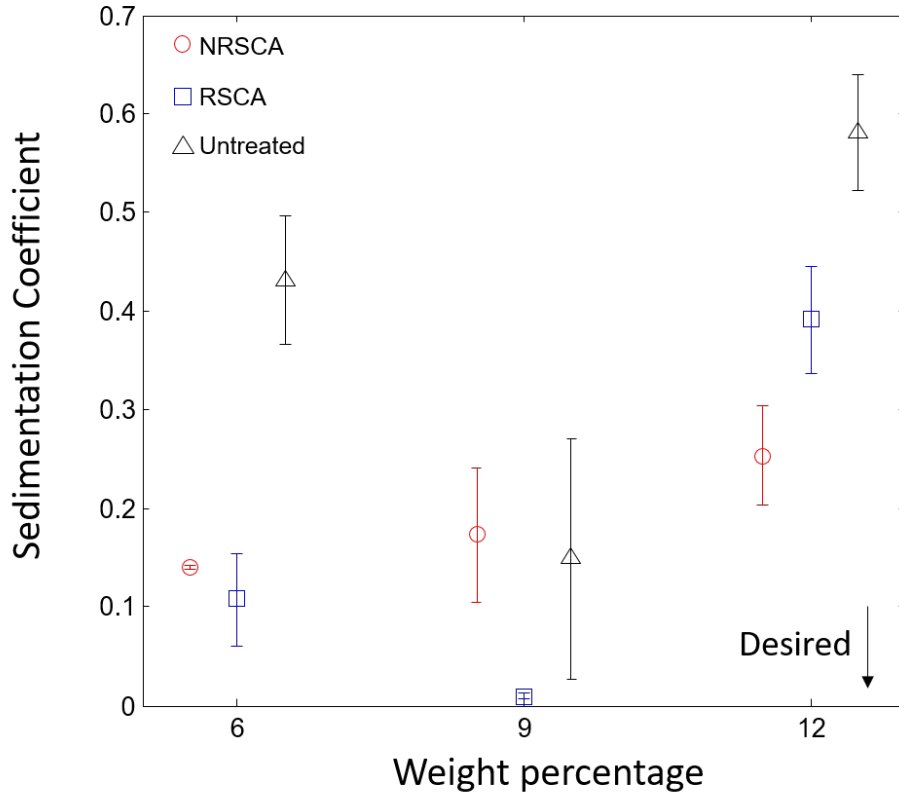


Figure 4.9: Sedimentation coefficient for each sample calculated by comparing difference in surface intensities between samples

The calculation of fractional changes in alumina content was then developed to be the difference in surface integrals for both sides divided by the average surface intensity value between both sides [15]. This work adjusts the formulation, with the removal of the multiplier, in order to set the range of possible values from 0 to 1. This relationship is shown in Equation 4.3.

$$S = \left| \frac{I_A - I_B}{\bar{I}} \right| = \left| \frac{I_A - I_B}{I_A + I_B} \right| \quad (4.3)$$

Figure 4.9 shows the sedimentation coefficients for all samples. Similar to the variance plots, a lower coefficient corresponds to reduced levels of sedimentation and is desired. In this case, the average sedimentation between both sets are plotted with range bars indicating the sedimentation coefficient for each individual sample. In every case, the application of surface treatment reduces the level of sedimentation. Furthermore, sedimentation is seen to be minimal in the 9 wt% sample which agrees with previous work [3]. This improvement in sedimentation at 9 wt% is again hypothesized to result from the effect of particle loading on flow properties of the resin which is hypothesized to affect the dispersion of particles during resin infusion.

4.3 Conclusions

This chapter undertook the quantitative and qualitative analysis of particle dispersion for hybrid carbon fiber composites. The first section presented the contour maps for the PL dispersion measurements of each hybrid carbon fiber composite. It was found from inspection that the treated samples had lower average intensity variations between regions on the surface of the samples. Quantitative analysis was then undertaken through the use of the variance to mean ratio for dispersion comparisons. Values for the VMR of all samples are presented in Table 4.1. It is found that the surface treatment improves the dispersion of particles and mitigates the large variations in dispersion behavior caused by different levels of particle loading. Furthermore, the RSCA treatment was found to provide for the most consistent dispersion of particles regardless of weight percentage.

Table 4.1: VMR for all tested samples. Lowest values for each surface treatment is bolded.

NRSCA											
6 wt%				9 wt%				12 wt%			
78.03	77.44	48.14	89.00	302.6	162.68	107.51	105.99	471.99	657.96	102.62	279.40
RSCA											
6 wt%				9 wt%				12 wt%			
153.75	58.83	82.67	166.64	174.63	276.17	97.8	178.28	163.48	279.17	447.42	243.48
Untreated											
6 wt%				9 wt%				12 wt%			
227.79	234.44	568.14	353.31	167.38	252.14	73.38	65.913	1072.2	445.07	1219.6	233.15

Levels of sedimentation were also analyzed using a previously developed sedimentation coefficient [3]. Values for the sedimentation coefficient of all samples are presented in Table 4.2. It is found that the 9 wt% samples have the lowest sedimentation regardless of surface treatment. Furthermore, the RSCA generally has the lowest sedimentation at the lower and intermediate particle loadings. The combined dispersion and sedimentation comparisons show that the RSCA treatment is capable of producing the most homogeneous distribution of particles, both on each individual face and between both faces. The NRSCA treatment can also be utilized for the production of more homogeneous samples; however, there is a greater variability dependent on the manufacturing parameters. Future mechanical tests will show the effects of this improved dispersion on the mechanical properties of the HCFRP materials.

Table 4.2: Sedimentation coefficient values for all tested samples. Lowest coefficient value for each treatment type is bolded.

NRSCA					
6 wt %		9 wt%		12 wt%	
0.142	0.138	0.241	0.105	0.304	0.202
RSCA					
6 wt%		9 wt%		12 wt%	
0.154	0.061	0.013	0.006	0.337	0.446
Untreated					
6 wt%		9 wt%		12 wt%	
0.365	0.496	0.271	0.027	0.640	0.522

CHAPTER 5

PARTICLE BONDING INVESTIGATION

High resolution photoluminescence measurements coupled with high magnification microscopy images are capable of providing information on particle bonding. Interlaminar shear strength improvements in hybrid fiber composites with functionalized fillers has been hypothesized to result from a variety of mechanisms. One particular mechanism is particle bonding to the organic sizing on the fibers effectively bridging the fiber and matrix. This mechanism was previously characterized by the agglomeration of functionalized nanotubes around fiber surfaces [81, 82]. Investigation into this mechanism is necessary in order to determine whether particle/fiber bonding occurs, and what the effects are on the stress state of the material. This work investigates similar regions of the composites with different surface treatments and presents the stress distributions of particles in these micro-regions.

The results of these investigations are presented as a micrograph image with the marked scanning region alongside the corresponding intensity, stress, and peak width contour maps. For this work, the results of interest are the stress and peak width distributions. Dispersion characterization cannot be performed due to the low depth of field of the microscope objective used. As a result, any differences in the particle depth from the top of the sample contributes an extra variable to the intensity distribution which cannot be removed. This depth difference is expected to be significant as the carbon fibers which are focused on are much larger than the particles and the laser spot size. This focusing issue is shown in figure 5.1. The stress and

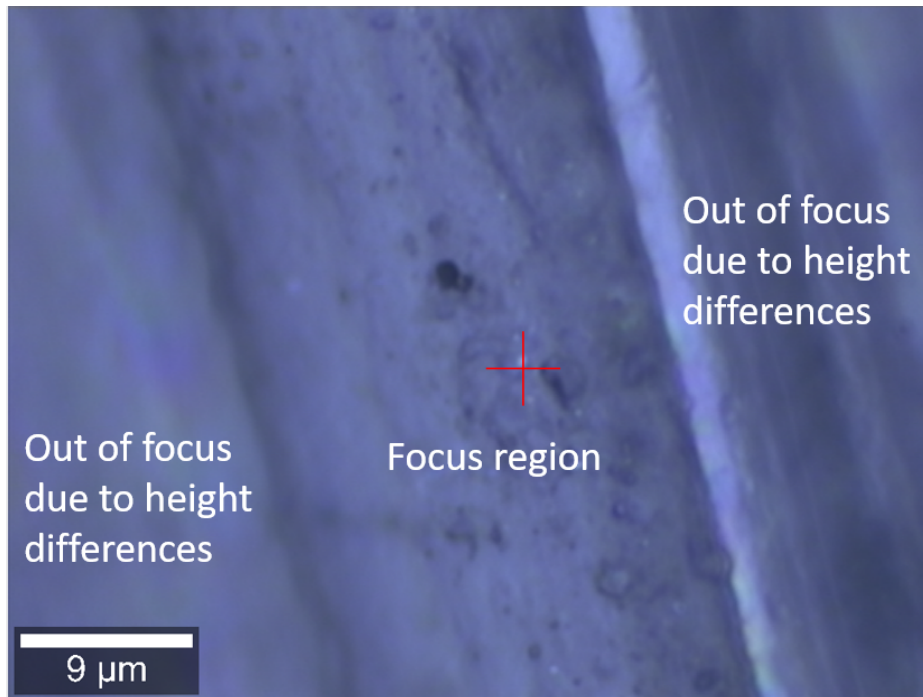


Figure 5.1: Micrograph image focused on single fiber shows outer matrix regions as being out of focus.

width values do not depend on the focusing distance and so different locations can instead be compared by those values.

5.1 Untreated Particle Behavior

The results from the high resolution investigation are presented in Figure 5.2. The f and m markings correspond to fiber and matrix regions. The boundaries of these regions are selected through optical analysis and are not exact. They instead simply serve to show any differences in particle behavior contained in a specific region. It is seen that the stress does not vary significantly with location of the investigated particle. This conclusion can be made from the

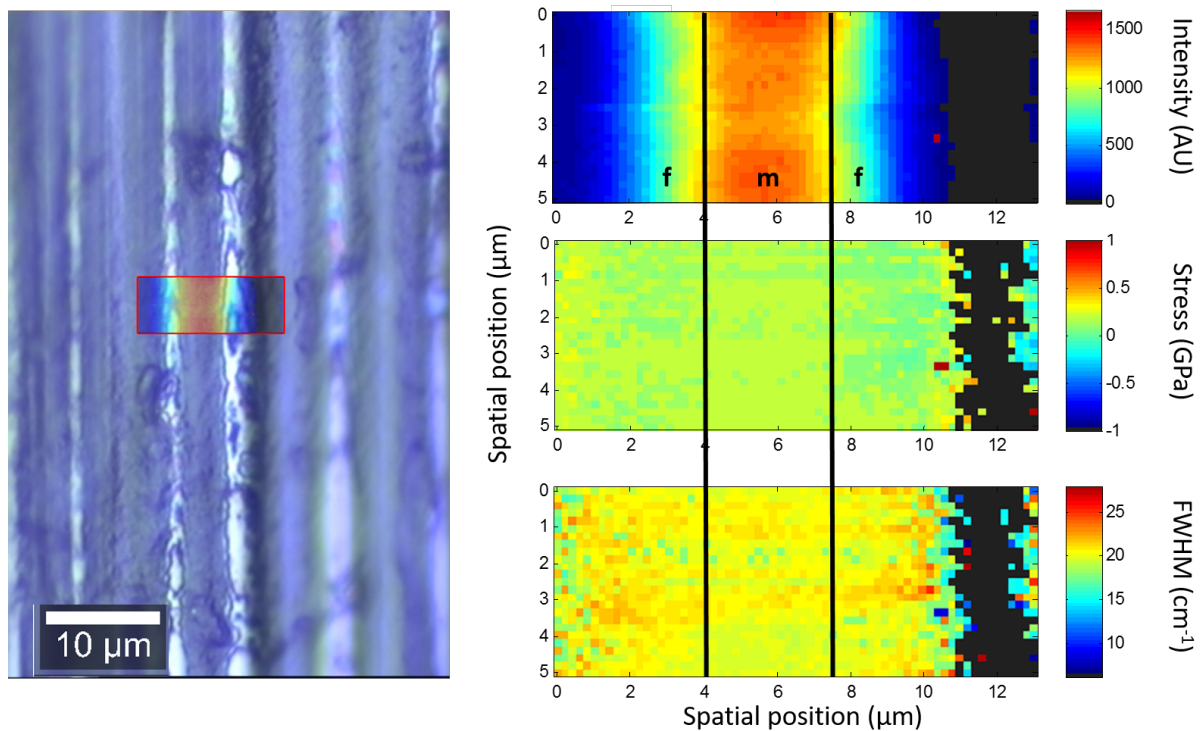


Figure 5.2: Residual stress behavior of particles treated with no surface treatment. a) Micrograph image overlaid with intensity plots showing particle alignment with fiber direction and b) (top) Intensity gradients correlating with (middle) hydrostatic residual stress gradients and (bottom) FWHM gradients homogeneous distribution of stress and width independent from the intensity variations. This indicates that the particles experience solely matrix bonding, and that the stress is distributed homogeneously in this region. The residual tensile stress state in the matrix resulting from the curing induced stress is hypothesized to transfer to the particles resulting in the values measured. This residual tensile stress in the matrix occurs from the limiting of the volumetric shrinkage associated with the polymerization reaction by the carbon fibers [83, 23, 33]. These results serve as a baseline for understanding the behavior of particles with applied surface treatments.

5.2 Functionalization of Particles for Adjustment of Bonding Behavior

Investigations of particle bonding can now be accomplished through the comparison of the stress contour maps for the surface treated particles. The first treatment investigated is the NRSCA surface treatment which is presented in Figure 5.3. The stress values and width values are again seen to be independent of particle location. This is explained by the bonding mechanism of particles with the NRSCA treatment, which is an adhesion bond similar to the bonding present in the untreated samples. It is noted that in most cases, the magnitudes of particle stress are increased with the NRSCA treatment. This can be explained by the improved compatibility of the organic coating with the organic matrix providing for improved load transfer of the residual stress to the particle.

The RSCA treatment, results of which are presented in Figure 5.4, show deviations from the previously noted behavior. In this case, there is a clear stress gradient which tends to match the intensity distribution. The magnitudes of the stress gradient are also extremely significant; in this work, a shift from a tensile stress state to a compressive stress state is detected. This is proposed to result from load transfer of the carbon fiber compressive residual stress to the particles through covalent bonding. Stress variations due to the location of the particles were detected in some cases in the other treatment types; however, the only samples which experienced compressive stresses in the particles were the RSCA treated ones.

The distribution of peak widths in these samples also provides important information. As previously stated, the peak widths are proportional to the deviatoric stress tensor [50]. As a re-

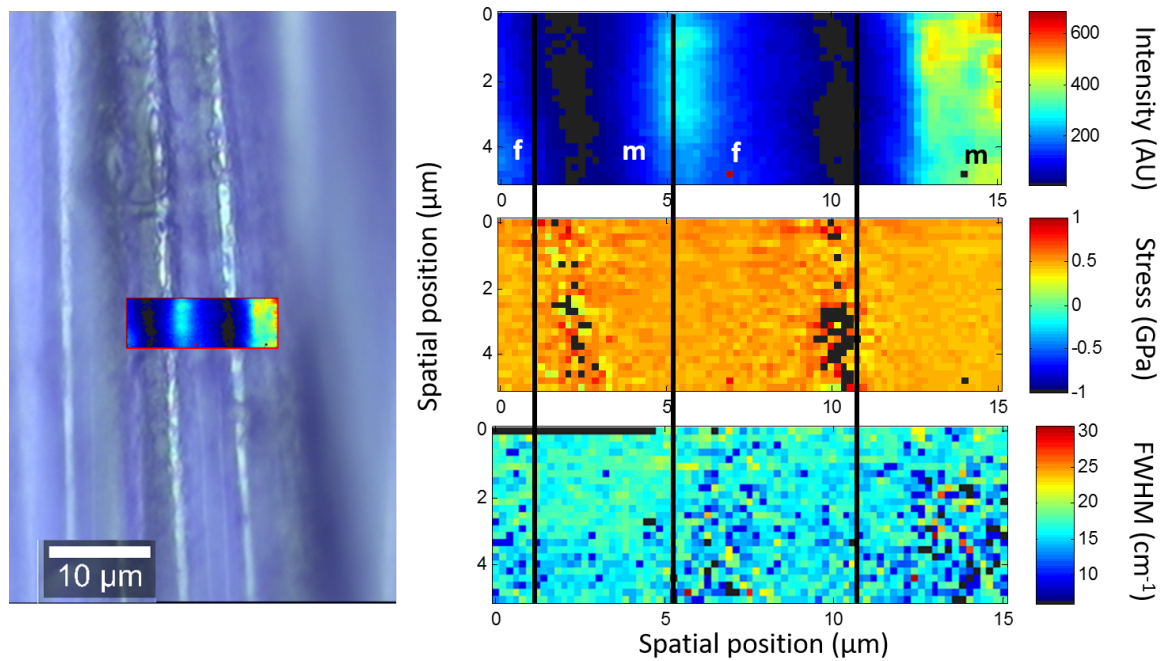


Figure 5.3: Residual stress behavior of particles treated with NRSCA surface treatment. a) Micrograph image overlaid with intensity plots showing particle alignment with fiber direction and b) (top) Intensity gradients correlating with (middle) hydrostatic residual stress gradients and (bottom) FWHM gradients

sult, broadening is noticed with increasing magnitudes of applied deviatoric stress. It is evident through comparison of the stress and width distributions, that the highly compressive regions are also characterized by much wider peaks. This is proposed to result from simultaneous fiber-matrix bonding which imparts a highly complex stress state on the particles. As a result of this stress state, it is likely that the stress will be distributed unevenly resulting in the noted broadening.

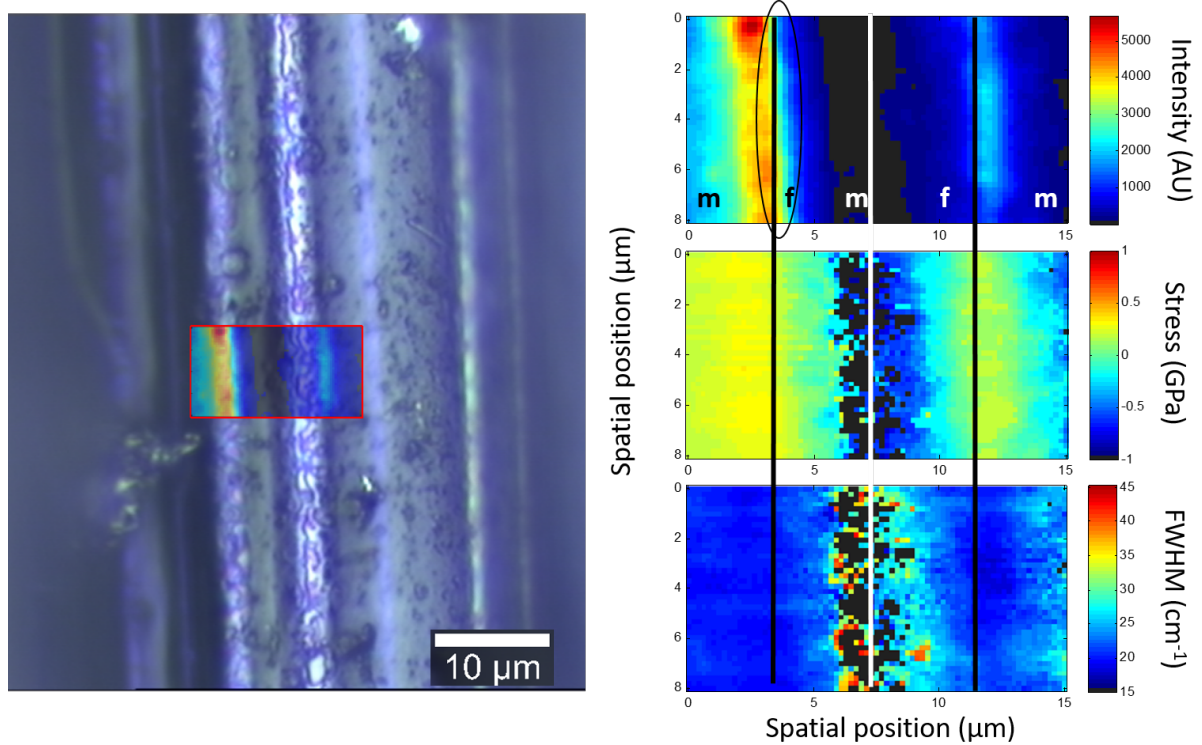


Figure 5.4: Residual stress behavior of particles treated with RSCA surface treatment. a) Micrograph image overlaid with intensity plots showing particle alignment with fiber direction and b) (top) Intensity gradients correlating with (middle) hydrostatic residual stress gradients and (bottom) FWHM gradients.

This fiber-matrix bridging by the particles is expected to provide improvements to material properties through improved bonding of fibers to matrix, effectively serving as an interphase. Silanized materials have previously been used as an interphase in hybrid carbon fiber composites for the improvement of interlaminar shear strength, flexural strength, and flexural modulus [38]. This offers another pathway for material property improvement. By utilizing this RSCA treatment it is expected that the strength of the material will increase by what can be referred to as anchoring of the fibers to the matrix preventing the early development of failure

mechanisms such as fiber pullout. Crack deflection will also occur around the fibers as a result of the hard and well bonded particles [82].

5.3 Conclusion

Investigations at higher resolutions characterized bonding behavior of nanoparticles with different surface treatments. Particles with reactive surface treatments were found to experience a change in hydrostatic stress from tension to compression with proximity to the carbon fibers. This is proposed to result from particle bonding to the carbon fiber sizing as a result of a compatibility of organic groups. The lack of this stress behavior in the untreated and NRSCA treated particles reinforces this hypothesis. Investigations of width distributions found that particles in the compressive region had broader emissions when compared to particles in the tensile zones. This is hypothesized to result from fiber-matrix bridging through particle bonding, which imparts a highly complex stress state to the particles. This bonding is expected to further increase mechanical properties of the composites due to stronger bonding of fibers to matrix through the particle intermediaries.

CHAPTER 6 CONCLUSION

In this work, manufacturing parameter effects on particle dispersion are presented. The parameters investigated, through photoluminescence spectroscopy, are levels of particle loading and the type of surface treatment. It was found that the application of silane coupling agents to the nanoparticles provided for improved dispersion. Furthermore, these treatments tended to provide for more consistent dispersion regardless of weight percentage. It is seen that the application of the surface treatment helps to remove variability of the composite samples which occur as a result of the manufacturing technique. Future work will apply this understanding to create more homogenous bulk composites. The variance to mean ratio is also utilized as a measure of dispersion and is found to allow for direct numeric comparisons which match the qualitative analysis.

Microscale investigations were also conducted on the 12 wt% samples. It was found, through R-line peak shift analysis, that the nanoparticles with RSCA treatments exhibited stress states dependent on proximity to the carbon fibers. This is proposed to result from compatibility of organofunctional groups in the reactive surface treatment with the organic sizing on the fibers. This behavior is not dependent on distribution of particles as similar zones investigated in the untreated and non-reactive treated samples had homogeneous stress distributions. Compressive regions measured in the RSCA were associated with region of R-line broadening, which is indicative of increased deviatoric stress. This is hypothesized to result from a

three way bond between fiber, matrix, and particle which is expected to improve mechanical properties.

Future mechanical testing will show the effects of the surface treatments and dispersion on the mechanical properties of the composites [18]. Through the use of piezospectroscopy combined with the mechanical testing, local features and their effects on stress can then be measured and quantified. Optimal manufacturing parameters can then be established based on mechanical properties, dispersion, and stress sensitivity [18]. This will benefit future investigation into hybrid carbon fiber composites for the purpose of the creation of next generation materials for various structural applications.

LIST OF REFERENCES

- [1] I. Hanhan, A. Selimov, D. Carolan, A. Taylor, and S. Raghavan, “Characterizing Mechanical Properties of Hybrid Alumina Carbon Fiber Composites with Piezospectroscopy,” in *57th AIAA/ASCE/AHS/ASC Structures, Structural Dynamics, and Materials Conference*, p. 1413, 2016.
- [2] A. Mohanty, V. K. Srivastava, and P. U. Sastry, “Investigation of mechanical properties of alumina nanoparticle-loaded hybrid glass/carbon-fiber-reinforced epoxy composites,” *Journal of Applied Polymer Science*, vol. 131, no. 1, pp. 1–7, 2014.
- [3] I. Hanhan, A. Selimov, S. Raghavan, D. Carolan, and A. Taylor, “Quantifying alumina nanoparticle dispersion in hybrid carbon fiber composites using photo-luminescent spectroscopy,” *Applied Spectroscopy*, vol. In Press, 2016.
- [4] A. Manero, A. Selimov, Q. Fouliard, K. Knipe, J. Wischek, C. Meid, A. M. Karlsson, M. Bartsch, and S. Raghavan, “Piezospectroscopic Evaluation and Damage Identification for Thermal Barrier Coatings Subjected to Simulated Engine Environments,” *Surface and Coatings Technology*, 2016.
- [5] WITec, “alpha300 RA Raman system.”
- [6] G. Freihofer, A. Schülzgen, and S. Raghavan, “Damage Mapping with a Degrading Elastic Modulus Using Piezospectroscopic Coatings,” (*submitted for publication*), 2015.

- [7] D. J. Bray, P. Dittanet, F. J. Guild, A. J. Kinloch, K. Masania, R. A. Pearson, and A. C. Taylor, "The modelling of the toughening of epoxy polymers via silica nanoparticles: The effects of volume fraction and particle size," *Polymer Journal*, vol. 54, no. 26, pp. 7022–7032, 2013.
- [8] V. Kushvaha and H. Tippur, "Effect of filler shape, volume fraction and loading rate on dynamic fracture behavior of glass-filled epoxy," *Composites Part B: Engineering*, vol. 64, pp. 126–137, 2014.
- [9] X. L. Ji, J. K. Jing, W. Jiang, and B. Z. Jiang, "Tensile modulus of polymer nanocomposites," *Polymer Engineering and Science*, vol. 42, no. 5, pp. 983–993, 2002.
- [10] S. C. Zunjarrao, R. Sriraman, and R. P. Singh, "Effect of processing parameters and clay volume fraction on the mechanical properties of epoxy-clay nanocomposites," *Journal of Materials Science*, vol. 41, no. 8, pp. 2219–2228, 2006.
- [11] M. H. G. Wichmann, J. Sumfleth, F. H. Gojny, M. Quaresimin, B. Fiedler, and K. Schulte, "Glass-fibre-reinforced composites with enhanced mechanical and electrical properties - Benefits and limitations of a nanoparticle modified matrix," *Engineering Fracture Mechanics*, vol. 73, no. 16, pp. 2346–2359, 2006.
- [12] E. Vassileva and K. Friedrich, "Epoxy/alumina nanoparticle composites. II. Influence of silane coupling agent treatment on mechanical performance and wear resistance," *Journal of Applied Polymer Science*, vol. 101, no. 6, pp. 4410–4417, 2006.

- [13] I. Isik, U. Yilmazer, and G. Bayram, "Impact modified epoxy/montmorillonite nanocomposites: synthesis and characterization," *Polymer Journal*, vol. 44, pp. 6371–6377, 2003.
- [14] A. L. Stevenson, *CALIBRATION OF ALUMINA-EPOXY NANOCOMPOSITES USING PIEZOSPECTROSCOPY FOR THE DEVELOPMENT OF STRESS-SENSING ADHESIVES*. PhD thesis, University of Central Florida, 2011.
- [15] I. Hanhan, *Hybrid Carbon Fiber Alumina Nanocomposite for Non-Contact Stress Sensing via Piezospectroscopy*. Honors in the Major thesis, University of Central Florida, 2015.
- [16] C. Soutis, "Carbon fiber reinforced plastics in aircraft construction," *Materials Science and Engineering A*, vol. 412, no. 1, pp. 171–176, 2005.
- [17] Y. Xu and S. V. Hoa, "Mechanical properties of carbon fiber reinforced epoxy/clay nanocomposites," *Composites Science and Technology*, vol. 68, pp. 854–861, 2008.
- [18] A. Selimov, D. Carlona, A. Taylor, and S. Raghavan, "Characterization of dispersion in hybrid carbon fiber composites through photoluminescence spectroscopy," *In preparation*, 2016.
- [19] Z. Guo, T. Pereira, O. Choi, Y. Wang, and H. T. Hahn, "Surface functionalized alumina nanoparticle filled polymeric nanocomposites with enhanced mechanical properties," *Journal of Materials Chemistry*, vol. 16, no. 27, p. 2800, 2006.
- [20] K. P. Gadkaree, "Particulate-fibre-reinforced glass matrix hybrid composites," *Journal of Materials Science*, vol. 27, no. 14, pp. 3827–3834, 1992.

- [21] M. Hussain, A. Nakahira, and K. Niihara, "Mechanical property improvement of carbon fiber reinforced epoxy composites by Al₂O₃ filler dispersion," *Materials Letters*, vol. 26, no. 3, pp. 185–191, 1996.
- [22] J. M. Long, X. Qin, and G. F. Wang, "Influence of surface energy on the elastic compression of nanosphere," *Journal of Applied Physics*, vol. 117, no. 5, pp. 1–7, 2015.
- [23] S. F. Ferdous, M. F. Sarker, and A. Adnan, "Role of nanoparticle dispersion and filler-matrix interface on the matrix dominated failure of rigid C60-PE nanocomposites: A molecular dynamics simulation study," *Polymer (United Kingdom)*, vol. 54, no. 10, pp. 2565–2576, 2013.
- [24] E. P. Plueddemann, *Silane Coupling Agents*. New York; London: Plenum Press, 2nd ed. ed., 1991.
- [25] S. Sterma and J. Marsden, "Silane Coupling Agents," *Industrial & Engineering Chemistry*, vol. 58, no. 3, pp. 33–37, 1966.
- [26] H. Ishida and J. L. Koenig, "The Reinforcement Mechanism of Fiber - Glass Reinforced Plastics Under Wet Conditions : A Review," *Polymer and Engineering*, vol. 18, no. 2, pp. 128–145, 1978.
- [27] E. P. Plueddemann, "Adhesion Through Silane Coupling Agents," *The Journal of Adhesion*, vol. 2, no. 3, pp. 184–201, 1970.

- [28] E. P. Plueddemann and G. Fanger, "Epoxyorganosiloxanes," *Journal of the American Chemical Society*, vol. 81, no. 11, pp. 2632–2635, 1959.
- [29] S. Y. Fu, X. Q. Feng, B. Lauke, and Y. W. Mai, "Effects of particle size, particle/matrix interface adhesion and particle loading on mechanical properties of particulate-polymer composites," *Composites Part B: Engineering*, vol. 39, no. 6, pp. 933–961, 2008.
- [30] J. R. Condon and J. L. Ferracane, "Reduced polymerization stress through non-bonded nanofiller particles," *Biomaterials*, vol. 23, no. 18, pp. 3807–3815, 2002.
- [31] Z. Demjén, B. Pukánszky, and J. Nagy, "Evaluation of interfacial interaction in polypropylene/surface treated CaCO₃ composites," *Composites Part A: Applied Science and Manufacturing*, vol. 29, no. 3, pp. 323–329, 1998.
- [32] W. D. Callister and D. G. Rethwisch, *Materials science and engineering: an introduction*. John Wiley & Sons, Inc., 8 ed., 2010.
- [33] O. Prejzek, M. Spaniel, and T. Mares, "Microstructural residual stress in particle-filled dental composite," *Comput Methods Biomech Biomed Engin*, vol. 18, no. 2, pp. 124–129, 2015.
- [34] R. R. Braga, R. Y. Ballester, and J. L. Ferracane, "Factors involved in the development of polymerization shrinkage stress in resin-composites: A systematic review," *Dental Materials*, vol. 21, no. 10, pp. 962–970, 2005.

- [35] C. L. Davidson and a. J. Feilzer, "Polymerization shrinkage and polymerization shrinkage stress in polymer-based restoratives.," *Journal of dentistry*, vol. 25, no. 6, pp. 435–440, 1997.
- [36] B. Pukánszky, "Interfaces and interphases in multicomponent materials: Past, present, future," *European Polymer Journal*, vol. 41, no. 4, pp. 645–662, 2005.
- [37] K. S. Wilson and J. M. Antonucci, "Interphase structure-property relationships in thermoset dimethacrylate nanocomposites," *Dental Materials*, vol. 22, no. 11, pp. 995–1001, 2006.
- [38] L. Chen, H. Jin, Z. Xu, M. Shan, X. Tian, C. Yang, Z. Wang, and B. Cheng, "A design of gradient interphase reinforced by silanized graphene oxide and its effect on carbon fiber/epoxy interface," *Materials Chemistry and Physics*, vol. 145, no. 1-2, pp. 186–196, 2014.
- [39] J. D. Barnett, S. Block, and G. J. Piermarini, "An optical fluorescence system for quantitative pressure measurement in the diamond-anvil cell," *Review of Scientific Instruments*, vol. 44, no. 1, pp. 1–9, 1973.
- [40] R. J. Christensen, D. M. Lipkin, and D. R. Clarke, "Nondestructive evaluation of the oxidation stresses through thermal barrier coatings using Cr^{3+} piezospectroscopy," *Applied Physics Letters*, vol. 69, p. 3754, 1996.

- [41] A. Stevenson, A. Jones, and S. Raghavan, "Stress-Sensing Nanomaterial Calibrated with Photostimulated Luminescence Emission," *Nano Letters*, vol. 11, no. 8, pp. 3274–3278, 2011.
- [42] G. Freihofer, J. Dustin, H. Tat, A. Schülzgen, and S. Raghavan, "Stress and structural damage sensing piezospectroscopic coatings validated with digital image correlation," *AIP Advances*, vol. 5, no. 3, p. 037139, 2015.
- [43] B. Henderson and G. F. Imbusch, *Optical spectroscopy of inorganic solids*. Oxford University Press, 2006.
- [44] L. Grabner, "Spectroscopic technique for the measurement of residual stress in sintered Al₂O₃," *Journal of Applied Physics*, vol. 49, no. 2, pp. 580–583, 1978.
- [45] D. Dragoman and M. Dragoman, *Optical Characterization of Solids*. Springer, 2002.
- [46] H. Hough, J. Demas, T. O. Williams, and H. N. G. Wadley, "Luminescence Sensing of Stress in Ti/Al₂O₃ Fiber Reinforced Composites," *Acta Metallurgica et Materialia*, vol. 43, no. 2, pp. 821–834, 1995.
- [47] M. Yourdkhani and P. Hubert, "Quantitative dispersion analysis of inclusions in polymer composites," *ACS Applied Materials and Interfaces*, vol. 5, no. 1, pp. 35–41, 2013.
- [48] C. J. Chang, L. J. Xu, Q. Huang, and J. J. Shi, "Quantitative characterization and modeling strategy of nanoparticle dispersion in polymer composites," *Iie Transactions*, vol. 44, no. August 2014, pp. 523–533, 2012.

- [49] D. J. Bray, S. G. Gilmour, F. J. Guild, T. H. Hsieh, K. Masania, and A. C. Taylor, "Quantifying nanoparticle dispersion: application of the Delaunay network for objective analysis of sample micrographs," *Journal of Materials Science*, vol. 46, no. 19, pp. 6437–6452, 2011.
- [50] Q. Ma and D. R. Clarke, "Stress Measurement in Single-Crystal and Polycrystalline Ceramics using their Optical Fluorescence," *Journal of the American Ceramic Society*, vol. 76, no. 6, pp. 1433–1440, 1993.
- [51] Q. Ma and D. R. Clarke, "Piezospectroscopic Determination of Residual Stresses in Polycrystalline Alumina," *Journal of American Ceramic Society*, vol. 77, no. 2, pp. 298–302, 1994.
- [52] J. He, I. J. Beyerlein, and D. R. Clarke, "Load transfer from broken fibers in continuous fiber Al_2O_3 -Al composites and dependence on local volume fraction," *Journal of the Mechanics and Physics of Solids*, vol. 47, no. 3, pp. 465–502, 1999.
- [53] X. Peng and D. R. Clarke, "Piezospectroscopic analysis of interface debonding in thermal barrier coatings," *Journal of the American Ceramic Society*, vol. 83, no. 5, pp. 1165–1170, 2000.
- [54] J. He and D. R. Clarke, "Determination of the Piezospectroscopic Coefficients for Chromium-Doped Sapphire," *J. Am. Ceram. Soc.*, vol. 78, no. 5, pp. 1347–1353, 1995.

- [55] J. He, I. J. Beyerlein, and D. R. Clarke, "Load transfer from broken fibers in continuous fiber Al₂O₃-Al composites and dependence on local volume fraction," *Journal of the Mechanics and Physics of Solids*, vol. 47, no. 3, pp. 465–502, 1999.
- [56] I. Hanhan, E. Durnberg, G. Freihofer, P. Akin, and S. Raghavan, "Portable Piezospectroscopy system: non-contact in-situ stress sensing through high resolution photoluminescent mapping," *Journal of Instrumentation*, vol. 9, no. 11, p. P11005, 2014.
- [57] R. Paschotta, "Fluence," 2008.
- [58] G. J. Freihofer, *Nanocomposite Coating Mechanics via Piezospectroscopy*. Doctoral dissertation, University of Central Florida, 2014.
- [59] S. Raghavan, P. K. Imbrie, and W. A. Crossley, "Spectral analysis of R-lines and vibronic sidebands in the emission spectrum of ruby using genetic algorithms," *Applied Spectroscopy*, vol. 62, no. 7, pp. 759–765, 2008.
- [60] G. K. Wertheim, M. A. Butler, K. W. West, and D. N. E. Buchanan, "Determination of the Gaussian and Lorentzian content of experimental line shapes," *Review of Scientific Instruments*, vol. 45, no. 11, pp. 1369–1371, 1974.
- [61] A. Selcuk and A. Atkinson, "Analysis of the Cr³⁺ luminescence spectra from thermally grown oxide in thermal barrier coatings," *Materials Science and Engineering A*, vol. 335, no. 1-2, pp. 147–156, 2002.

- [62] T. H. Hsieh, A. J. Kinloch, K. Masania, J. Sohn Lee, A. C. Taylor, and S. Sprenger, “The toughness of epoxy polymers and fibre composites modified with rubber microparticles and silica nanoparticles,” *Journal of Materials Science*, vol. 45, no. 5, pp. 1193–1210, 2010.
- [63] I. Nanomaterials, “alfa- Aluminum Oxide (Alumina) nano powder, 99.8%, 40 nm grain size, APS 150 nm.”
- [64] M. Gilbert, *Carbon Fibre Composites with Alumina Nanoparticles for Stress Sensing*. PhD thesis, Imperial College London, 2015.
- [65] J. Kim, M. Kim, and K. Ha, “New ultrasonic dispersion method for nanoparticles using cylindrical piezoelectric transducer,” *Proceedings - IEEE Ultrasonics Symposium*, vol. 0, no. 1, pp. 2072–2075, 2010.
- [66] Gurit, “UT-C400 Uni-directional Reinforcement Fabric datasheet.”
- [67] J. Wang, “Machinability study of polymer matrix composites using abrasive waterjet cutting technology,” *Journal of Materials Processing Technology*, vol. 94, no. 1, pp. 30–35, 1999.
- [68] H. S. Sas, P. Šimáček, and S. G. Advani, “A methodology to reduce variability during vacuum infusion with optimized design of distribution media,” *Composites Part A: Applied Science and Manufacturing*, vol. 78, pp. 223–233, 2015.

- [69] K. L. White, P. Li, H. Yao, R. Nishimura, and H. J. Sue, "Effect of surface modifier on flow properties of epoxy suspensions containing model plate-like nanoparticles," *Rheologica Acta*, vol. 53, no. 7, pp. 571–583, 2014.
- [70] R. Mathur, D. Heider, C. Hoffmann, J. W. Gillespie, S. G. Advani, and B. K. Fink, "Flow front measurements and model validation in the vacuum assisted resin transfer molding process," *Polymer composites*, vol. 22, no. 4, pp. 477–490, 2001.
- [71] Hoel, "On indices of dispersion," *The Annals of Mathematical Statistics*, vol. 14, no. 2, pp. 155–162, 1943.
- [72] A. Clapham, "Over-Dispersion in Grassland Communities and the Use of Statistical Methods in Plant Ecology A," *Journal of Ecology*, vol. 24, no. 1, pp. 232–251, 1936.
- [73] V. V. Bhanu Prasad, B. V. R. Bhat, P. Ramakrishnan, and Y. R. Mahajan, "Clustering probability maps for private metal matrix composites," *Scripta Materialia*, vol. 43, no. 9, pp. 835–840, 2000.
- [74] A. Slipenyuk, V. Kuprin, Y. Milman, J. E. Spowart, and D. B. Miracle, "The effect of matrix to reinforcement particle size ratio (PSR) on the microstructure and mechanical properties of a P/M processed AlCuMn/SiCp MMC," *Materials Science and Engineering A*, vol. 381, no. 1-2, pp. 165–170, 2004.
- [75] P. J. Clark and F. C. Evans, "Distance to Nearest Neighbor as a Measure of Spatial Relationships in Populations," *Ecology*, vol. 35, no. 4, pp. 445–453, 1954.

- [76] M. C. Kissinger-Kane, *Investigation and Characterization of the Dispersion of Nanoparticles in a Polymer Matrix by Scattering Techniques*. PhD thesis, University of Florida, 2007.
- [77] A. Yazdanbakhsh, Z. Grasley, B. Tyson, and R. K. Abu Al-Rub, “Dispersion quantification of inclusions in composites,” *Composites Part A: Applied Science and Manufacturing*, vol. 42, no. 1, pp. 75–83, 2011.
- [78] M. D. Haslam and B. Raeymaekers, “A composite index to quantify dispersion of carbon nanotubes in polymer-based composite materials,” *Composites Part B: Engineering*, vol. 55, no. 1, pp. 16–21, 2013.
- [79] M. Morisita, “Measuring of the dispersion of individuals and analysis of the distributional patterns,” *Memoirs of the Faculty of Science, Kyushu University, Series E*, vol. 2, no. 4, pp. 215–235, 1959.
- [80] G. Patil and W. Stiteler, “Concepts of aggregation and their quantification: A critical review with some new results and applications,” *Resources in Population Ecology*, vol. 15, no. 1, pp. 238–254, 1974.
- [81] F. H. Gojny, M. H. G. Wichmann, B. Fiedler, W. Bauhofer, and K. Schulte, “Influence of nano-modification on the mechanical and electrical properties of conventional fibre-reinforced composites,” *Composites Part A: Applied Science and Manufacturing*, vol. 36, no. 11, pp. 1525–1535, 2005.

- [82] M. M. Rahman, S. Zainuddin, M. V. Hosur, C. J. Robertson, A. Kumar, J. Trovillion, and S. Jeelani, "Effect of NH 2-MWCNTs on crosslink density of epoxy matrix and ILSS properties of e-glass/epoxy composites," *Composite Structures*, vol. 95, pp. 213–221, 2013.
- [83] M. Y. Quek, "Analysis of residual stresses in a single fibre-matrix composite," *International Journal of Adhesion and Adhesives*, vol. 24, no. 5, pp. 379–388, 2004.